MASTER

Nuclear spin lattice relaxation time measurements : an experimental set-up

Denissen, C.J.M.

Award date:
1982

NUCLEAR SPIN LATTICE RELAXATION TIME

MEASUREMENTS

C.J.M. Denissen

An experimental set-up

picture 1   Hence you long-legged spinners, hence!

Contents:

Summary

In this report an experimental equipment for measuring the nuclear spin lattice relaxation time T_1 is described. The nuclear spin lattice relaxation time yields information about the dynamics of the electron spin system in a magnetic insulator. In view of the recent theoretical development on non-linear excitations (solitons) in one-dimensional magnetic systems, it is very interesting to investigate the influence of non-linear excitations on the dynamics of quasi 1d-magnetic systems experimentally. For this reason we decided to build an experimental set-up for measuring T_1.

In the experimental method the T_1 is determined by measuring the recovery of the nuclear magnetization. The magnetization recovers exponentially towards its equilibrium value with a characteristic time T_1. The recovery of the nuclear magnetization is measured with aid of the spin-echo technique. A theoretical description of the spin-echo according to Hahn is given. Special attention is given to the impedance matching of the total electronic circuit in order to obtain an optimal performance of the experimental equipment. A cryogenic system is designed which allows us to measure the T_1 in the temperature range 1.2 K < T < 300 K. In order to test the experimental set-up we performed experiments on paraffin. The spin-echo signal in paraffin behaved in agreement with the theory of Hahn for spin-echo. From the T_1 measurements of paraffin it followed that we could measure T_1 with an accuracy of 10%. In conclusion we can say that the experimental equipment works satisfactory.

A start is made with the investigation of the linear excitations in 1d-magnetic systems. Measurements were performed on the nuclear spin lattice relaxation time T_1 of ^1H and ^{133}Cs in the quasi 1d-Ising antiferromagnets $RbFeCl_3.2H_2O$ and $CsFeCl_3.2H_2O$. A preliminary interpretation of the measured data on basis of a soliton theory is given. It appears that for high temperatures (T > 20 K) the results can be explained satisfactory with this soliton theory.

CHAPTER 1   INTRODUCTION

In the group "Magnetische Ordeningsverschijnselen" (cooperative phenomena) we are interested in cooperative and collective phenomena in systems in the solid state which consist of many particles which have mutual interactions. Magnetic systems appear to be very suitable to investigate these kind of phenomena. The interacting particles in magnetic systems are microscopic magnetic moments (spins). In general the interactions between the moments are important in all three spatial directions. Because the phenomena become enormously complicated in three dimensional magnetic systems we have to restrict ourselves to more simple systems. The most simple magnetic systems in which the moments have mutual interactions is a magnetic chain. Although in nature there exist no magnetic chains, many magnetic systems exist in which the moments have in one direction a much larger interaction than in the other two directions, the so called quasi one-dimensional systems.

Much theoretical and experimental research is done on the static properties of these systems such as the susceptibility, resonance phenomena as nuclear magnetic resonance (N.M.R.), antiferromagnetic resonance (A.F.M.R.) and spin cluster resonance, specific heat and phase diagrams. Although the static properties of quasi one-dimensional magnetic systems are understood quite well, the knowledge of the dynamical properties is small. In view of the recent theoretical development on non-linear dynamics (solitons) in 1D-magnetic systems, it is very interesting to investigate the dynamics of quasi 1D-systems.

The dynamics of a magnetic system is reflected in several physical quantities such as the heat conductivity, neutron diffraction, mössbauer linewidth, nuclear spin lattice relaxation time T_1, etc. As the nuclear spin lattice relaxation time, T_1 is a very powerful tool for studying such non-linear excitations and a part of the necessary apparatus for measuring T_1 was already present in the group we decided to build an experimental equipment for measuring T_1.

My work in my final year was to build and test such a experimental apparatus. At the end a start was made with measuring the T_1 of the protons in quasi 1d Ising antiferromagnets in order to study the predicted contribution due to solitons in T_1 (ref. 13).

In the first part of this report an introduction of the nuclear spin lattice relaxation time is given (chapter 2). In chapter 3 the

experimental method and the theory of Hahn for spin-echo is treated. In the next chapter the experimental apparatus is described. In chapter 5 the results of testmeasurements on paraffin are given and compared with theoretical expectations from the theory of Hahn for spin-echo. In the last chapter results of the measurements of the ^{1}H and ^{133}Cs nuclear spin lattice relaxation time of the Ising antiferromagnets $RbFeCl_3 \cdot 2H_2O$ (RFC) and $CsFeCl_3 \cdot 2H_2O$ (CFC) are given.

Chapter 2   Introduction of the nuclear spin lattice relaxation time

2.1 Introduction

As mentioned already in the introduction (chapter 1) we are interested in the nuclear spin lattice relaxation time T_1 in magnetic insulators because it gives us information about the dynamics of the electron spins in these compounds. Before paying attention to the complicated relaxation processes which take place in magnetic insulators (section 2.3) we will first introduce the relaxation time by examening a simple proton system coupled with a reservoir (section 2.2) .

Because T_1 can be measured by making use of the motion of the magnetization M of the nuclear spins, we treat the equations of motion for M. After we first treat the motion of M for free spins in a static magnetic field (section 2.4) and a small alternating field (section 2.5) , we give in section 2.6 the general equations of motion for the magnetization M of the nuclear spins.

2.2 Relaxation in an ensemble of protons coupled with a reservoir

In this section we introduce the relaxation time T_1 by examining a simple magnetic system, i.e. an ensemble of N protons which is coupled with a simple reservoir. The protons have a magnetic moment $\vec{\mu} = -\gamma \hbar \vec{I}$ with $I = \frac{1}{2}$. For the present discussion the details of the coupling are not important. In general we can describe the protons and the reservoir with the following Hamiltonian:

$$\mathcal{H} = \mathcal{H}_p + \mathcal{H}_{pr} + \mathcal{H}_r \qquad 2.2.1$$

where $\mathcal{H}_p$ and $\mathcal{H}_r$ describe the proton system and the reservoir, respectively. $\mathcal{H}_{pr}$ describes the interaction between the protons and the reservoir. In our simple example we assume that there is no interaction between the protons. In that case the Hamiltonian $\mathcal{H}_p$ is given by:

$$\mathcal{H}_p = \sum_i \mathcal{H}_{pi} = \sum_i -\vec{\mu}_i \cdot \vec{H} , \qquad 2.2.2$$

where $\vec{H}$ is the magnetic field at the proton position.

It is well known that we can distinguish two states, $|+\frac{1}{2}\rangle$ $(m_s = +\frac{1}{2})$ and $|-\frac{1}{2}\rangle$ $(m_s = -\frac{1}{2})$ which are degenerated in a zero magnetic field. In a magnetic field these two states split and the energy difference between

the states is proportional to the field, $\Delta E = \gamma \hbar H_0$ (see fig. 2.2.1.).

$$H=0 \qquad N^- \underline{\qquad\qquad} |-\tfrac{1}{2}\rangle$$

$$\underline{\qquad\qquad\qquad} |+\tfrac{1}{2}\rangle, |-\tfrac{1}{2}\rangle \qquad \Delta E = \gamma \hbar H_0$$

$$N^+ = N^- = N/2 \qquad N^- \underline{\qquad\qquad} |+\tfrac{1}{2}\rangle$$
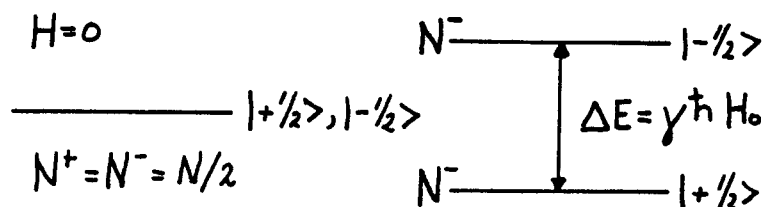
fig. 2.2.1   Energy levels of the proton system.

For simplicity we assume that the reservoir has two energy states $|a\rangle$ and $|b\rangle$, of which the energy spacing is the same as that of the proton system (see fig. 2.2.2.).
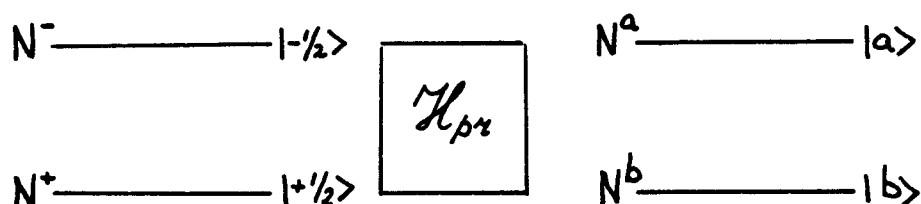
$$N^- \underline{\qquad\qquad} |-\tfrac{1}{2}\rangle \qquad \boxed{\mathcal{H}_{pr}} \qquad N^a \underline{\qquad\qquad} |a\rangle$$

$$N^+ \underline{\qquad\qquad} |+\tfrac{1}{2}\rangle \qquad\qquad N^b \underline{\qquad\qquad} |b\rangle$$

fig. 2.2.2   The proton system coupled with a simple two level reservoir.

If the coupling between the protons and the reservoir is small ($\mathcal{H}_{pr}$ is small) the states of the total system (protons and reservoir) can be characterised as follows $|+\tfrac{1}{2}a\rangle, |+\tfrac{1}{2}b\rangle, |-\tfrac{1}{2}a\rangle, |-\tfrac{1}{2}b\rangle$. The coupling between the proton system and the reservoir, $\mathcal{H}_{pr}$ can induce transitions between the states of the total system. Because energy must be conserved during a transition it is easily seen that the only possible transitions are $|-\tfrac{1}{2}b\rangle \rightarrow |+\tfrac{1}{2}a\rangle$ and $|+\tfrac{1}{2}a\rangle \rightarrow |-\tfrac{1}{2}b\rangle$. The probability per second that a transition takes place is according Fermi's golden rule as follows:

$$W_{|\tfrac{1}{2}a\rangle \rightarrow |-\tfrac{1}{2}b\rangle} = W_{|-\tfrac{1}{2}b\rangle \rightarrow |\tfrac{1}{2}a\rangle} = \tfrac{2\pi}{\hbar} \left| \langle -\tfrac{1}{2}b | \mathcal{H}_{pr} | \tfrac{1}{2}a \rangle \right|^2 \qquad 2.2.3$$

We now want to derive a differential equation for the change of the occupation number N^+ of the state $|+\tfrac{1}{2}\rangle$ of the proton system. Therefore we define the transition probabilities per second $W\downarrow$ and $W\uparrow$. $W\downarrow$ and $W\uparrow$ are the transition probabilities per sec. that the transitions $|-\tfrac{1}{2}\rangle \rightarrow |+\tfrac{1}{2}\rangle$ and $|+\tfrac{1}{2}\rangle \rightarrow |-\tfrac{1}{2}\rangle$, respectively take place. It is easily seen that $W\uparrow$ and $W\downarrow$ are given by:

$$W\uparrow = N^a \; W(|\tfrac{1}{2}a\rangle \rightarrow |-\tfrac{1}{2}b\rangle)$$
$$W\downarrow = N^b \; W(|-\tfrac{1}{2}b\rangle \rightarrow |\tfrac{1}{2}a\rangle) \qquad 2.2.4$$

where N^a, N^b are the occupation numbers of the states $|a\rangle$ and $|b\rangle$ of the reservoir, respectively.

Using $W\downarrow$ and $W\uparrow$ we obtain the following differential equation for the change of the population N^+:

$$dN^+/dt = N^- W\downarrow - N^+ W\uparrow \qquad 2.2.5$$

In thermal equilibrium dN^+/dt is zero and eq. 2.2.5. tells us, that the ratio of N_0^- and N_0^+ is equal to:

$$N_0^-/N_0^+ = W\uparrow/W\downarrow \qquad 2.2.6$$

At thermal equilibrium it is well known that the ratio of N_0^- and N_0^- is given by the Boltzmann factor (ref 1):

$$N_0^-/N_0^+ = exp-(\gamma \hbar H_0/kT) \qquad 2.2.7$$

where T is the temperature of the total system.

Equation 2.2.5 describes how N^+ reaches its equilibrium value N_0^+. By defining the variables n, n_0, N and T_1:

$$\begin{aligned} n &= N^+ - N^- \\ n_0 &= N_0^+ - N_0^- \\ T_1 &= 1/(W\uparrow + W\downarrow) \end{aligned} \qquad 2.2.8$$

we can rewrite eq. 2.2.5 as follows:

$$d(n-n_0)/dt = -(n-n_0)/T_1 \qquad 2.2.9$$

The solution of eq. 2.2.9 is given by:

$$n = n_0 (1 - exp-(t/T_1)), \qquad 2.2.10$$

where we used the initial condition n(t=0)=0.

The recovery of n to its equilibrium value n_0 is called the nuclear spin lattice relaxation process. T_1 is the characteristic time associated with the approach to thermal equilibrium. T_1 is the so called "nuclear spin lattice relaxation time". From equation 2.2.8 we see that T_1 is determined by $W\uparrow$ and $W\downarrow$. Because $W\uparrow$ and $W\downarrow$ contain information about the reservoir (see matrixelements, eq. 2.2.3), the T_1 gives us information about the reservoir.

Because the nuclear magnetization M is proportional to n, the equations
2.2.9 and 2.2.10 also hold for the magnetization M.
We have assumed in this introduction that the proton system was inter-
acting with a reservoir. In the next section we will introduce the mag-
netic insulator and we will give a scheme of the most important inter-
actions in the magnetic insulator.

2.3 Survey of the relaxation phenomena in a magnetic insulator.

In the former section we introduced the relaxation time in an ensemble
of protons coupled wit a reservoir. We showed that the relaxation pro-
cess of the proton system was possible because it was coupled with the
reservoir.
We now introduce relaxation processes in a more complicated system, the
magnetic insulator. However, before we can start with this, we have to
know what systems we can distinguish in the magnetic insulator and how
they are coupled with each other. Because magnetic insulators consist
of nuclei, ions and atoms which are located on well defined positions
in the lattice we can distinguish in general three subsystems in a mag-
netic insulator.

     1 the crystal: atoms, ions which form the lattice

     2 the electron spin system: the moments (spins) of atoms which
       have an incomplete subshell resulting in a angular momentum J

     3 the nuclear spin system: the moments of nuclei which have a
       resulting angular momentum I (for protons $I=\frac{1}{2}$).

In section 2.2 we showed that the interaction of the proton system with
the reservoir made a relaxation process of the proton system possible.
In fig. 2.3.1 the most important interactions between the subsystems
of the magnetic insulator are shown in a schematic survey.
Because the lattice, the electron spin system, the nuclear spin system
and the surroundings are coupled they are in thermal equilibrium.
We first will consider the nuclear spin system. IN general the nuclear
spin system in the insulator is directly coupled with the electron spin
system and the lattice. If we apply a magnetic field H_o, the occupation
numbers of the energy states of the nuclear spin system will change un-
til a new equilibrium occupation is reached. Because the macroscopic

nuclear magnetization is determined by the occupation of the energy levels, it will also change until the equilibrium value of the magnetization $M_0 = \chi H_0$ is reached. This process is called the nuclear spin lattice relaxation process and is described by (see section 2.6):

$$M = M_0 \left(1 - exp -[t/T_1] \right) \qquad 2.3.1$$

The characteristic time in which the equilibrium magnetization is reached is called the nuclear spin lattice relaxation time T_1.
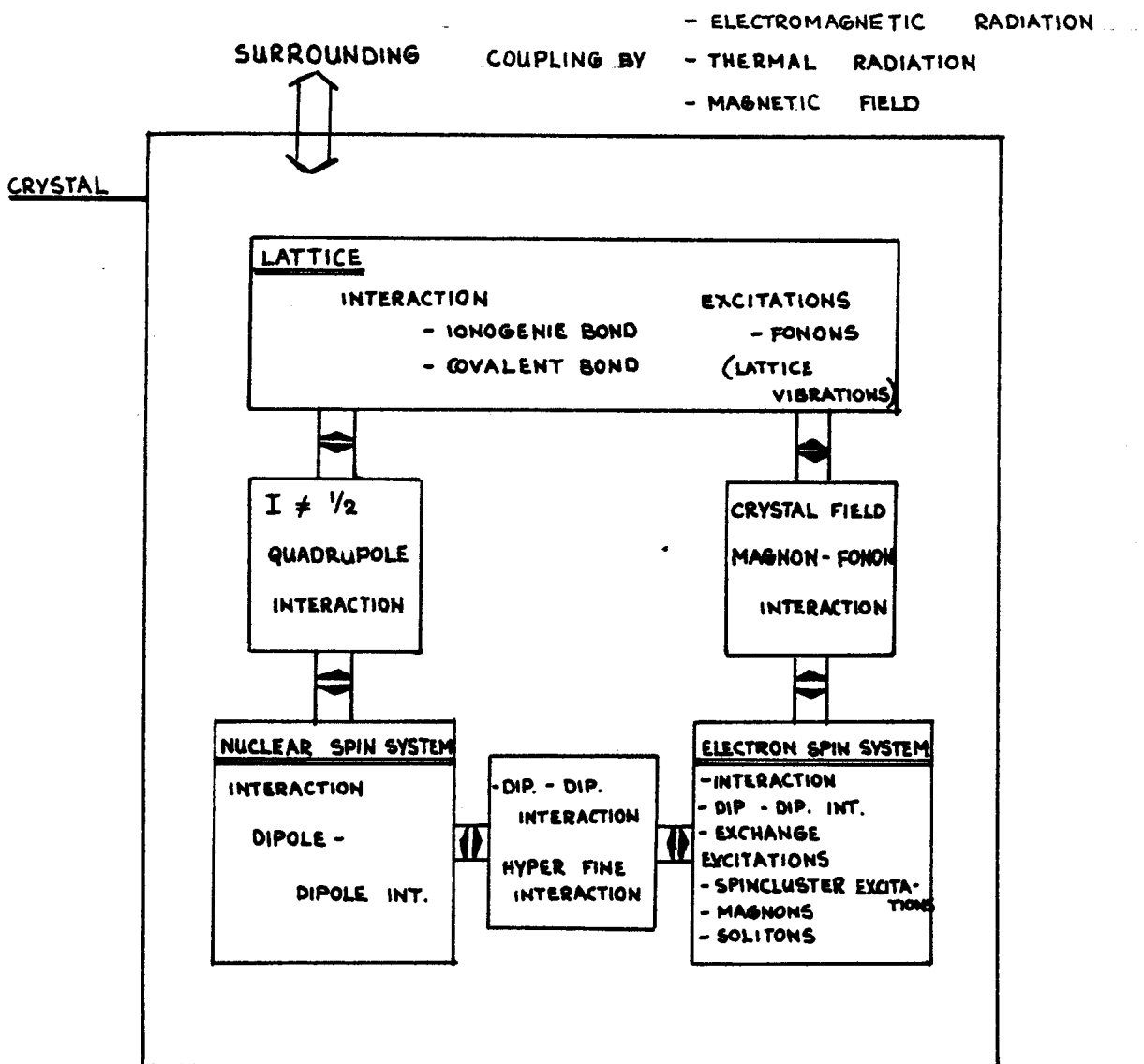

fig. 2.3.1 Scheme of interactions within and between the seperate subsystems of a magnetic insulator (ref 3).

For a nuclear system consisting of protons which have a spin quantum number $I=\frac{1}{2}$, the spins are only coupled with the electron spin system as there is no quadrupole interaction. The interactions which play a significant role are the hyperfine interaction (ref 5) and/or the dipole-dipole interaction (ref 6). In the former section we showed that T_1 depends on the energy states of the reservoir which is in this case the electron spin system. So we can use T_1 for studying the dynamics of the electron spin system.

In the same way as we did for the nuclear spin system we can consider the electron spin system and introduce a relaxation process for the electron spin system. The characteristic time for this relaxation process is called the electron spin lattice relaxation time. Because this time depends on the energy states of the electron spin system, it is possible to use it also for studying the dynamics of the electron spin system (ref 4).

In the former part we introduced a relaxation process of the nuclear spin system and electron spin system with an other system. Within the nuclear spin system and the electron spin sytem the moments are also coupled with each other. Because of this coupling the nuclear and electron spin system will be in internal equilibrium. If the systems are not in internal equilibrium, thermal equilibrium will be reached through relaxation processes within the nuclear, electron spin system. The characteristic time in which internal equilibrium is reached is called the spin-spin relaxation time (ref 7).

In section 2.6 . we will treat the equation of motion of the magnetization of the nuclear spins because the T_1 plays an important role in this equation. In chapter 3 we show that we can measure the nuclear spin lattice relaxation time with aid of this equation.

2.4 Motion of an isolated spin in a static magnetic field

Before we treat the general equation of motion of the nuclear magne-
tization as proposed by Bloch (section 2.6), we first give a description
of the motion of a magnetic moment $\vec{\mu}$ in a static magnetic field $\vec{H}_0$.
According to classical mechanics this equation of motion is given by (ref 2):

$$d\vec{\mu}/dt = \gamma \vec{\mu} \times \vec{H}_0 \qquad 2.4.1$$

where γ is the gyromagnetic ratio.

In order to solve this equation we transform it to a rotating coordinate
system S' that is rotating with respect to the laboratory system with
the angular frequency $\vec{\omega}$. According to the general law of relative motion
the time derivative $\frac{d\vec{A}}{dt}$ of any time dependent vector $\vec{A}(t)$ in the laboratory
frame S is related to the time derivative $\frac{\partial\vec{A}}{\partial t}$ in the rotating frame S'
in the following way:

$$d\vec{A}/dt = \partial\vec{A}/\partial t + \vec{\omega} \times \vec{A} \qquad 2.4.2$$

This relation yields for the equation of motion in the rotating frame S':

$$\partial\vec{\mu}/\partial t = \gamma \vec{\mu} \times \left(\vec{H}_0 + \vec{\omega}/\gamma \right) \qquad 2.4.3$$

This equation 2.4.3 is of the same form as 2.4.1 provided we replace
the actual magnetic field H_0 by an effective field H_e:

$$\vec{H}_e = \vec{H}_0 + \vec{\omega}/\gamma \qquad 2.4.4$$

If we choose a rotating frame S' which rotates with $\vec{\omega} = -\gamma\vec{H}_0$, it follows
from equation 2.4.3 that $\partial\vec{\mu}/\partial t = 0$. In the rotating frame $\vec{\mu}$ is a fixed vec-
tor and in the laboratory frame it is precessing around the magnetic
field $\vec{H}_0$ with the angular frequency $\vec{\omega}_0$. ω_0 is called the Larmor frequency.
In the above part we treated the motion of a magnetic moment $\vec{\mu}$. For
an ensemble of spins we can define the magnetization $\vec{M}$ as follows:

$$M_\alpha = \sum_i \mu_{\alpha i} \quad , \quad with \quad \alpha = x, y, z \qquad 2.4.5$$
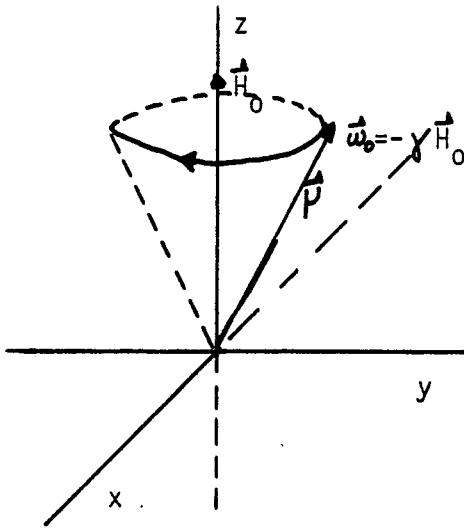
fig. 2.4.1 Precession of the magnetic moment with ω_0 in frame x,y,z.

If the spins have no interaction with each other and the surroundings, the equations for $\vec{\mu}$ are also valid for the magnetization M. Equation 2.4.1 becomes in this case:

$$d\vec{M}/dt = \gamma \vec{M} \times \vec{H_0} \qquad 2.4.6$$

In the following section we will treat the motion of the magnetization of isolated spins if a small alternating magnetic field perpendicular to the static magnetic field is applied.

2.5   Effect of an alternating magnetic field

In the former section we treated the motion of the magnetization in a static field $H_0(\vec{H_0}//z)$. In this section we will analyse the effect of a small alternating field $2H_1\cos\omega t$ perpendicular to the static field. We can treat this alternating field as a superposition of two fields, which are rotating in opposite directions with angular frequency $+\omega$ and $-\omega$, respectively as is shown in fig. 3.2.2.
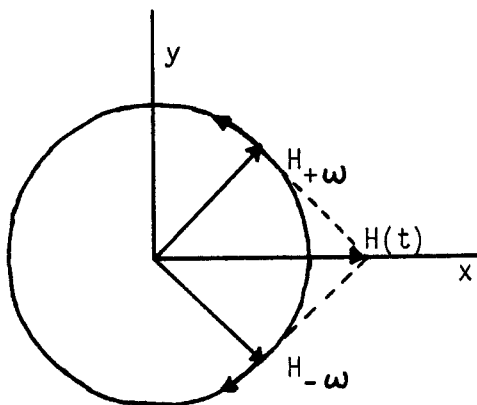

fig. 2.5.1 Decomposition of a linear oscillating field into two rotating components.

It can be shown (ref 9) that a small alternating field $\vec{H}_1$ perpendicular to the field $\vec{H}_0$ only has effect on the motion of the magnetization $\vec{M}$ if its angular frequency is equal to $\omega_0 = \gamma H_0$, the so called Larmor frequency. This is called the resonance condition. A quantum mechanical description also gives this resonance condition (ref 10). Furthermore it can be shown that only the component of H(t) which rotates with the angular frequency $-\vec{\omega_0}$ has influence on the magnetization (ref 9) . In a rotating frame S' which rotates at angular frequency $\vec{\omega_0} = -\gamma\vec{H}_0$ the motion of the magnetization is given by:

$$\partial M / \partial t = \vec{M} \times \gamma \vec{H}_e$$

2.5.1

$$\text{where } \vec{H}_e = \left(H_0 - {}^{\omega_0}/\gamma \right) e_z + H_1 e_{x'}$$

Using the relation $\omega_0 = \gamma H_0$ it follows that H_e is given by:

$$\vec{H}_e = H_1 e_{x'}$$

2.5.2

From eq. 2.5.1. and 2.5.2. it follows that the magnetization M precesses around H_1 with angular frequency $\vec{\omega_1} = -\gamma\vec{H}_1$ in the rotating frame S' as is shown in fig. 2.5.3.
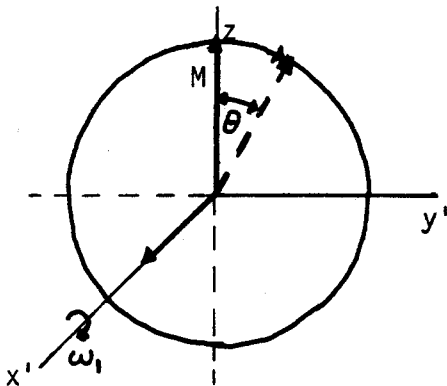
fig. 2.5.2   Precession of M around H_1 in the rotating frame S'. At t=0 M is directed along the z-direction.

In the laboratory coordinate system we obtain a combined motion of the precession around H_1 with angular frequency $\vec{\omega_1} = -\gamma\vec{H}_1$ and the precession around H_0 with angular frequency $\omega_0 = -\gamma\vec{H}_0$ as is shown in fig. 2.5.3.

fig. 2.5.3   Motion of the magnetization in the laboratorium frame S.
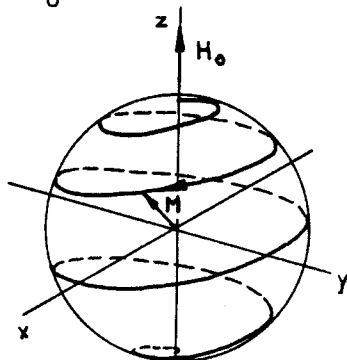
If we apply the alternating field $H_1(t)$ for a short time (that is, apply

a wave train of duration t_w), the magnetization M precesses through an angle $\theta = \gamma H_1 t_w$ (see fig. 2.5.3.). If t_w is chosen such that $\theta = \pi$, the pulse will simply invert the magnetization. Such a pulse is referred to in the literature as a "180 degree pulse" (π -pulse). For a "90 degree pulse" ($\pi/2$-pulse), the magnetization turns from the z-direction to the y'-direction.

The influence of an alternating field on the motion of the magnetization M is used in our experimental method.

In the next section we will describe the equations of the magnetization of nuclear spins with interactions as proposed by Bloch.

2.6 The equations of Bloch

In 1947 Felix Bloch proposed for the description of the magnetization of an ensemble of nuclei in a magnetic field a set of very simple equations derived from phenomenological arguments (ref 8). In this section we will describe these equations.

In a static field $H_z = H_0$ the recovery of the z-component of the nuclear magnetization towards its equilibrium value $M_z = M_0 = \chi H_0$ can often be described by the equation:

$$dM_z/dt = -\left[(M_z - M_0)/T_1\right], \qquad 2.6.1$$

where T_1 is the nuclear spin lattice relaxation time.

If the magnetization has transverse components, these components decay according the following equations:

$$dM_x/dt = -M_x/T_2 , \quad dM_y/dt = -M_y/T_2 \qquad 2.6.2$$

where T_2 is the transverse relaxationtime.

Equations 2.6.1 and 2.6.2 describe the change of the magnetization M of the nuclear spins due to interactions of the spins with each other and the surroundings. If we combine 2.6.1 and 2.6.2 with the equation which describes the motion of $\vec{M}$ in a magnetic field $\vec{H}$, which consists of a static magnetic field $\vec{H}_0$ and a small alternating field H(t) , we find:

$$d(M_z - M_0)/dt = -(M_z - M_0)/T_1 + (\vec{M} \times \gamma \vec{H})_z$$

$$d M_x / dt = -M_x/T_2 + (\vec{M} + \gamma \vec{H})_x \qquad 2.6.3$$

$$d M_y / dt = -M_y/T_2 + (\vec{M} + \gamma \vec{H})_y$$

In a static magnetic field $\vec{H}_0$ and for $\vec{M}=(M_0,0,0)$ at t=0, we obtain the following solution of eq. 2.6.3.:

$$M_z = M_0 (1 - exp-[t/T_1])$$

$$M_x = M_0 \, exp-[t/T_2] \, \cos \omega_0 t \qquad 2.6.4$$

$$M_y = M_0 \, exp-[t/T_2] \, \sin \omega_0 t$$

From this solution we see that M_z reaches the equilibrium value M_0 in a characteristic time T_1 as is shown in fig. 2.6.1.
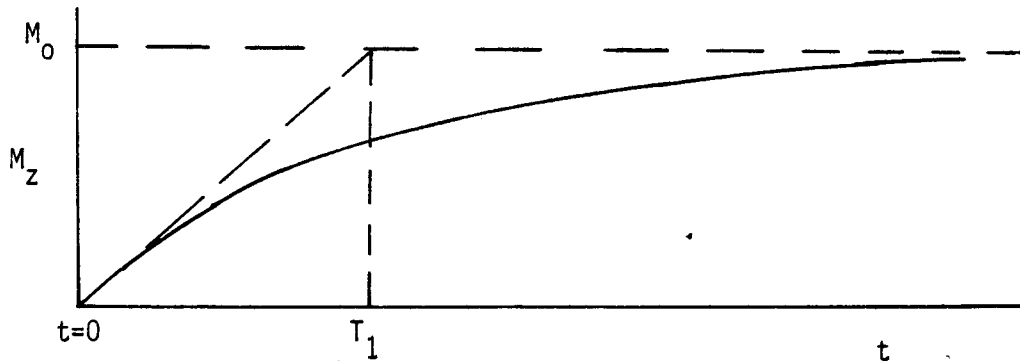

fig. 2.6.1   Exponential time dependence of the z-component of the mag-
netization.

The components M_x,M_y are decaying exponentially as is shown in fig. 2.6.2.
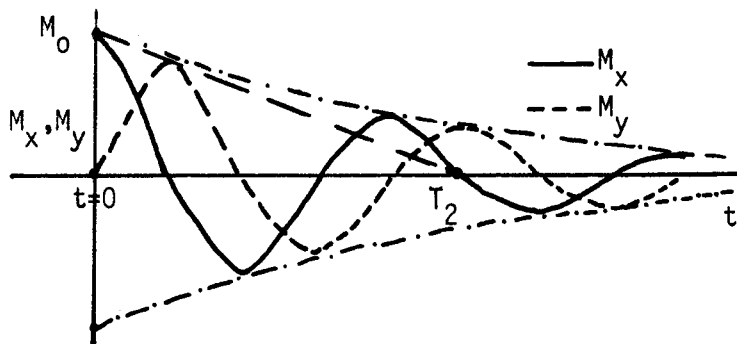

fig. 2.6.2   Exponential
decay of M_x,M_y.

In the next chapter we will explain the experimental method for measuring T_1. The Bloch equations will play an important role in understanding this experimental method.

Chapter 3 Experimental method

3.1. Introduction

In the former chapter we have given an introduction of the nuclear spin lattice relaxion time. We have also treated the equation of motion for the nuclear magnetization, because the time dependence of the magnetization is controlled by the nuclear spin lattice relaxation time T_1.
In this chapter we will describe an experimental method for measuring T_1. First we will describe the principles of the measurement.
If we apply at t=0 an external magnetic field H_0 to the nuclear spin system, this field establishes at thermal equilibrium a nuclear magnetization $M_0 = \chi H_0$ parallel to the field. We showed in chapter 2 that the equilibrium value of the magnetization M_0 is reached in a characteristic time T_1. If we assume that the magnetization M of the sample is zero at t=0, we obtain from the Bloch equations for $\vec{H}_0 /\!/ \vec{z}$:

$$M_z(t) = M_0 \left(1 - \exp-[t/T_1]\right)$$
$$M_x(t) = 0 \qquad\qquad 3.3.1$$
$$M_y(t) = 0$$

The magnetization Mz shows an exponential time dependence and the equilibrium value is $M_0 = \chi H_0$ as is shown in fig. 3.1.1.
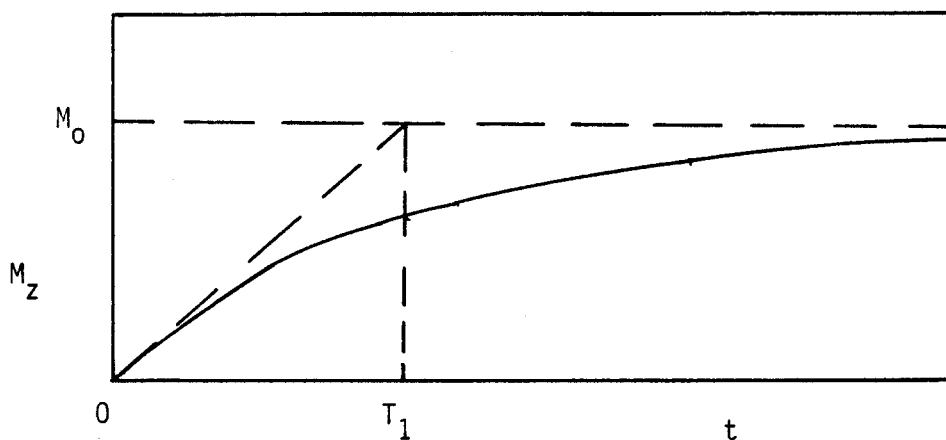

fig. 3.1.1   Exponential time dependence of the magnetization M_z, if at t=0 an external field is applied.

If we are able to measure the magnetization Mz as function of the time we can simply determine the relaxation time T_1. At equilibrium the magnetization Mz is Mo in an applied magnetic field. If we want to measure the exponential rise of the magnetization we must have a method to demagnetize the nuclear spin system in a static magnetic field. A method for demagnetizing the nuclear spin system and measuring the time dependence of Mz will be treated in this chapter. The method is based on the influence of an alternating field perpendicular to the static field on the motion of the magnetization (see &2.5).

In &3.2. we describe the experimental method for measuring the nuclear spin lattice relaxation time. In &3.3. we will give a theoretical description of the experimental method. We conclude this section with some general remarks.

3.2. Experimental method

In the introduction we concluded that we needed two things for measuring the nuclear spin lattice relaxation time T_1. First we have to demagnetize the nuclear spin system in a static magnetic field H_0 and secondly we must be able to measure the recovery of Mz as function of t. In fig. 3.3.2. we show two techniques which can be used for measuring T_1.

Before t=0 we apply in both cases a pulse sequence of pulses filled with the r.f. carrier of frequency ω_0 to a coil in which the sample is located (see fig. 3.2.1.). So during the pulses an alternating field is applied to the nuclear spin system. In this way we can saturate the nuclear spin system as will be shown in &3.3.1. This means that after the pulse sequence

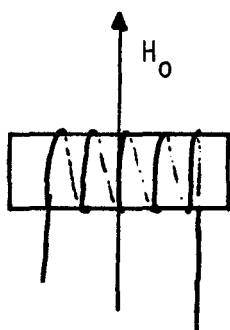
fig. 3.2.1   The coil in which a sample is located.

the nuclear magnetization of the nuclear spins has become zero. This pulse sequence is called the comb. After the comb (t=0) the nuclear magnetization is recovering to its equilibrium.

For measuring the recovery of Mz we can use two methods. In the first method we apply at t=T a 90 degree pulse ($\pi/2$ pulse) which turnes the magnetization
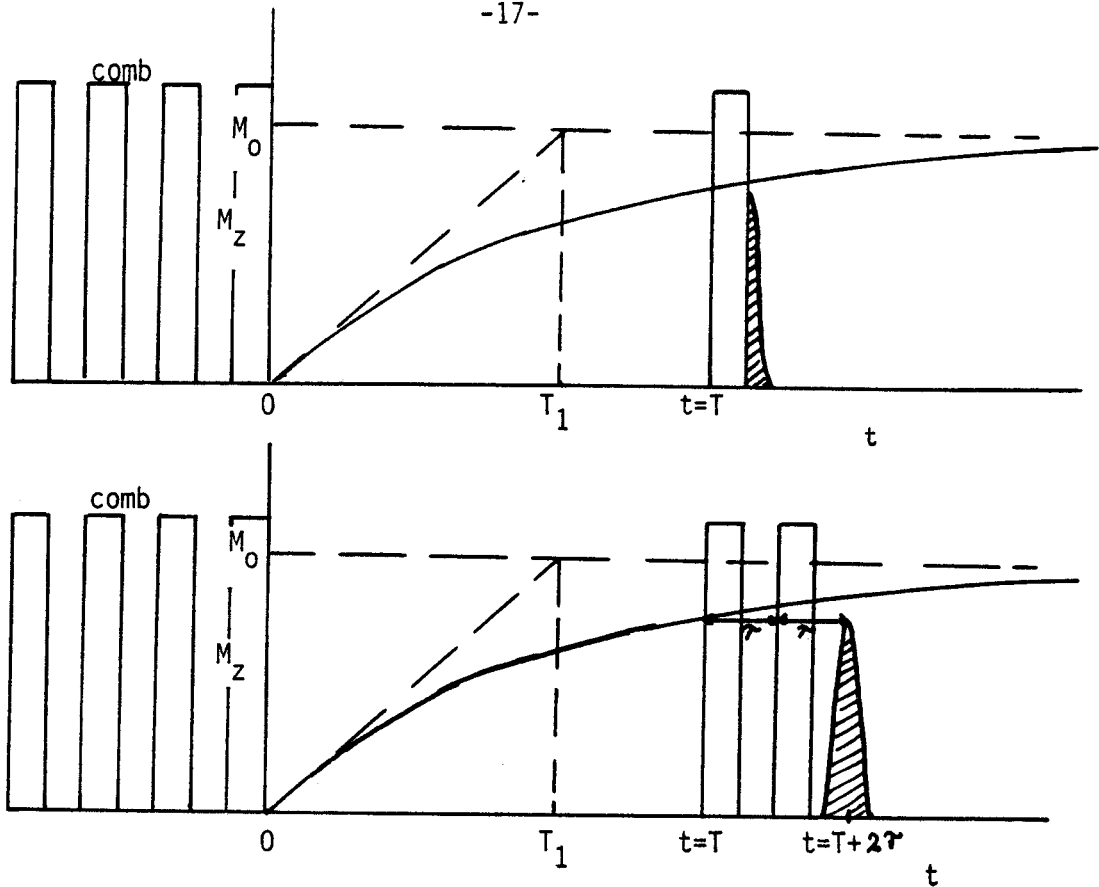
fig. 3.2.2   (a) Following the comb, M_z is recovering to M_o. At t=T
we apply a single $\pi/2$-pulse. After the pulse we obtain
a free induction signal which is proportional to $M_z(T)$.
       (b) At t=T we apply a double pulse. At t=T+2τ we obtain
an induction signal proportional to $M_z(T)$.

$M_z(T)$ in the xy-plane. After the pulse an electromotive force (emf) is
induced in the coil, which can be observed. This induction signal is
called free induction decay. The amplitude of the free induction decay
is proportional to $M_z(T)$. This will be explained in &3.3.2. and
&3.3.3.
In the second method we apply at t=T a pulse sequence of two $\pi/2$-pulses
with a distance τ between the pulses. We observe after the first pulse
a free induction decay and after the second pulse at t=T+2τ an induction
signal which is called spin-echo. The amplitude of the spin-echo signal
is proportional to $M_z(T)$. This will be explained in &3.3.2. and &3.3.3.
By repeating the above methods for several t=T we can measure the recovery
of Mz as function of T.

3.3. Theory of the experimental method

In &3.2. we described two methods to measure the nuclear spin lattice relaxation time. In this section we will describe the used techniques theoretically. In &3.3.1. we describe the saturation of the nuclear spin system. In &3.3.2. we treat a simple model for the free induction decay and spin-echo. Finally in &3.3.3. the results of a general analysis of free induction decay and spin-echo will be given.

3.3.1. Saturation of the nuclear spin system

In this section we treat the function of the comb. During the pulses of the comb an alternating field H_1 with frequency $\omega_0 = \gamma H_0$ is applied to the nuclear spin system. For understanding the function of the comb we use a quantum mechanical picture. We consider a nuclear spin system consisting of protons which have I=1/2 as introduced already in chapter 2. In a static external field H_0 the twofold degenerate energy levels are splitted as is shown in fig. 3.3.2.
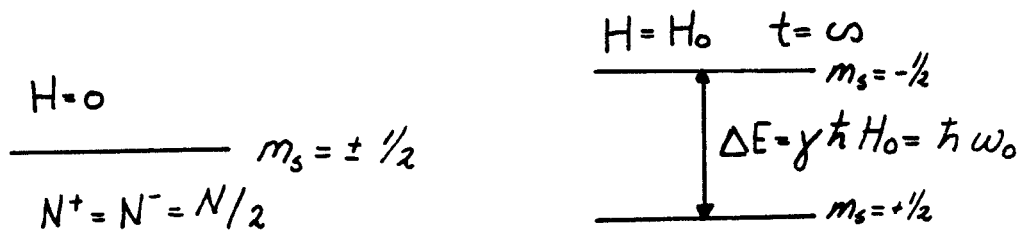
fig. 3.3.1 The energy levels of the proton system.

In thermal equilibrium the ratio of the occupation numbers N_0^+ and N_0^- is given by the Boltzmanfactor $N_0^-/N_0^+ = \exp{-\Delta E/kT}$. The difference in occupation $n_0 = N_0^+ - N_0^-$ gives rise to a macroscopic magnetization $M = M_0 = \chi H_0$. If we apply an alternating field with frequency ω_0 transitions are induced between the two states of the protons. According to Slichter (ref. 1) the change in n due to the alternating field is given by:

$$dn/dt = -2Wn + (n_0 - n)/T_1 \qquad 3.3.1$$

The solution of eq. (3.3.1.) is given by:

$$n = n_0/(2WT_1 + 1) + n_0/(1 + \tfrac{1}{2WT_1}) \exp{-[2W + 1/T_1]t} \qquad 3.3.2$$

In the steady state, eq. (3.3.2.) tells us that

$$n = n_0/(1 + 2WT_1),$$ 3.3.3

where W is the probability per second that a transition occurs due to the alternating field. W is proportional to the square of the field $(W \sim H_1^2)$.

If W is large enough $(W \gg 1/(2T_1))$ we see from eq. 3.3.3. that in the steady state n becomes zero and that means that the macroscopic magnetization M becomes zero. Because W is larger than $1/T_1$ $(W \gg 1/(2T_1))$ the steady state is reached in a characteristic time 1/2W(eq. 3.3.2.).

It can be shown that we can demagnetize a "general" nuclear magnetic system by applying a large enough alternating field. Instead of applying the alternating field continuously during t > 1/2W, we apply it in the form of the comb. The reason for this is that in practice the spectrum is not monochromatic (frequency ω_0) but has a certain linewidth due to field inhomogeneities. Because the frequency spectrum of a small wave train (1-5 µsec) is broader than of a long wave train ($\approx$ 20-80 µsec) we use a comb of small wave trains (Appendix C).

We have described a method for demagnetizing a nuclear spin system at t=0. In the next section we will describe the free induction decay and spin-echo using a simple vector model.

3.3.2. Simple model for free induction decay and spin-echo

In fig. 3.2.1. two methods were shown to measure the magnetization Mz at t=T. In this section we will show that the free induction decay and the spin echo are proportional to Mz(T). For convenience we would like to change to a new time variable t such that the new variable t, starts at zero at the beginning of the first pulse.

Not all the nuclear moments that contribute to the total magnetization M have the same precession frequency, because of the inhomogeneities in the magnetic field H_0.

For convenience we define macroscopic moment vectors M($\Delta\omega$) ($\Delta\omega = \omega - \omega_0$) where ω_0 is the centre frequency of the spectrum. M($\Delta\omega$) is the contribution to the total magnetization of all the nuclear moments that experience the same field (H=$\gamma\omega$) and therefore precess at the same Larmor frequency ω. The distribution of M($\Delta\omega$) is determined by the inhomogeneities in field H_0. We use the following notation for M($\Delta\omega$):

$$M(\Delta\omega) = M \, g(\Delta\omega)$$

with $$\int_{-\infty}^{+\infty} g(\Delta\omega) \, d(\Delta\omega) = 1$$ 3.3.4

In eq. 3.3.4 $g(\Delta\omega)$ describes the form of the spectrum. In first approximation we will use a rectangular spectrum $g(\Delta\omega)$ over $\Delta\omega = \omega - \omega_0$ as shown in fig 3.3.2.

$g(\Delta\omega)$

$-(\Delta\omega)_{\frac{1}{2}} \quad \omega_0 \quad (\Delta\omega)_{\frac{1}{2}} \quad \Delta\omega$
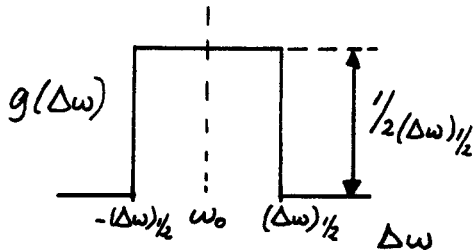
$\frac{1}{2}(\Delta\omega)_{\frac{1}{2}}$

fig. 3.3.2   Field inhomogeneities cause a distribution of the moment vectors $M(\Delta\omega)$. The spectrum $g(\Delta\omega)$ is assumed rectangular.

We will start with treating the free induction decay. For convenience we consider the magnetization in a rotating coordinate frame S', which rotates with the centre frequency of the spectrum. The magnetic moment vectors in the rotating frame S' are defined as:

$$M'(\Delta\omega) = \left(M_{x'}(\Delta\omega), M_{y'}(\Delta\omega), M_z(\Delta\omega) \right) \qquad 3.3.5$$

At t=0 we apply a $\pi/2$ pulse and the magnetization Mz is turned from the z-direction to the y'-direction (see fig. 3.3.3. A en B). After the pulse the various moment vectors $M'((\Delta\omega))$, $M'(-(\Delta\omega))$ will precess at frequency $\Delta\omega$ in the frame S', maintaining a symmetry around the y'-axis but rotating in opposite directions (fig. 3.3.3.C).
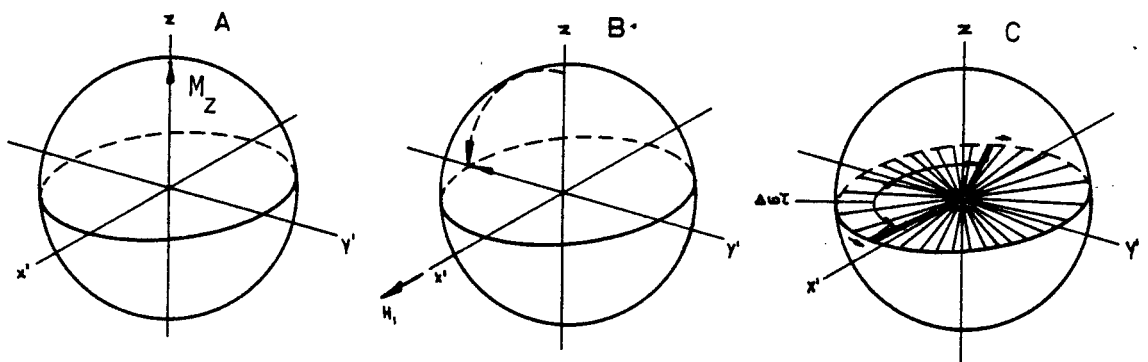
fig. 3.3.3   Formation of a free induction decay (in the rotating frame S').

So for the component Mx'(t) we obtain:

$$M_{x'}(t) = 0 \qquad 3.3.6$$

By solving the Bloch equation for My'(t,$\Delta\omega$) and integrating over all $\Delta\omega$, we obtain for My'(t):

$$M_{y'}(t) = -M_z \exp-[t/T_2] \frac{\sin\{(\Delta\omega)_{\frac{1}{2}}t\}}{(\Delta\omega)_{\frac{1}{2}}t} \qquad 3.3.7$$

In the calculations the duration of the pulse, t_w, is neglected because

we assumed that $t_w \ll T_2, 1/(\Delta\omega)_{1/2}$. For the above calculation the reader is referred to appendix B. In a coil along the y-direction in the laboratory frame S, the rotating magnetization M(t) given by,

$$M(t) \sim M_{y'}(t) \cos\omega_0 t \qquad 3.3.8$$

induces an induction voltage over the coil.

The induction voltage V(t) is proportional to dM/dt, so we obtain for V(t):

$$V(t) \sim \frac{d M_{y'}(t)}{dt} \cos\omega_0 t - M_{y'}(t)\omega_0 \sin\omega_0 t \qquad 3.39$$

Because $\omega_0 \gg 1/T_2$, $(\Delta\omega)_{1/2}$ we can neglect the first term and the amplitude of V(t) is given by:

$$V(t) \sim M_z \exp-[t/T_2] \frac{\sin\{(\Delta\omega)_{1/2} t\}}{(\Delta\omega)_{1/2} t} \qquad 3.3.10$$

This induction voltage is called the free induction decay. We see that it is proportional to Mz.

The decay of the induction voltage is determined by two terms, one depending on the T_2 and one on the width $(\Delta\omega)_{1/2}$ of the frequency spectrum $g(\Delta\omega)$.

In the next part of this section we will describe a simple model for the formation of the spin-echo. At t=0 the magnetization is given by Mz. Because the spin-echo is more complicated we neglect in first approximation the influence of the relaxationprocesses on the formation of the spin-echo. So we assume that $T_1, T_2 \gg \tau$, where τ is the distance between the two pulses.
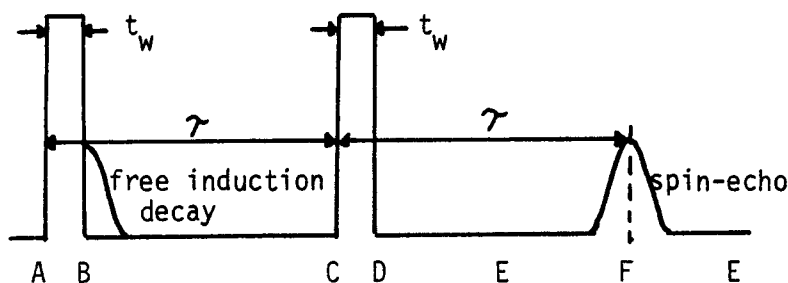

fig. 3.3.4   Free induction decay and spin-echo, if two $\pi/2$-pulses are applied.

At t=0 we apply a π/2-pulse. After the pulse we can observe a free induction decay which is given by eq. 3.3.9 with $T_2 = \infty$. At $t \gtrsim 2\pi/(\Delta\omega)_{1/2}$ this free induction decay is zero. At t=τ $(\tau > 2\pi/(\Delta\omega)_{1/2})$ we apply the second π/2-pulse which rotates the moment vectors from $\varphi = 3/2\pi \pm (\Delta\omega)\tau$, $\Theta = \pi/2$ to $\varphi(0)$, $\varphi(\pi)$, $\Theta = \pi-(\Delta\omega)\tau$, where Θ, φ are the spherical coordinates of the moment vectors (fig. 3.3.5. D). During the time $\tau < t < 2\tau$ all moment vectors $M'(\Delta\omega)$ interfere destructively over an unit sphere (fig. 3.3.5. E) until the time t=2τ when they interfere constructively. At time 2τ all the moment
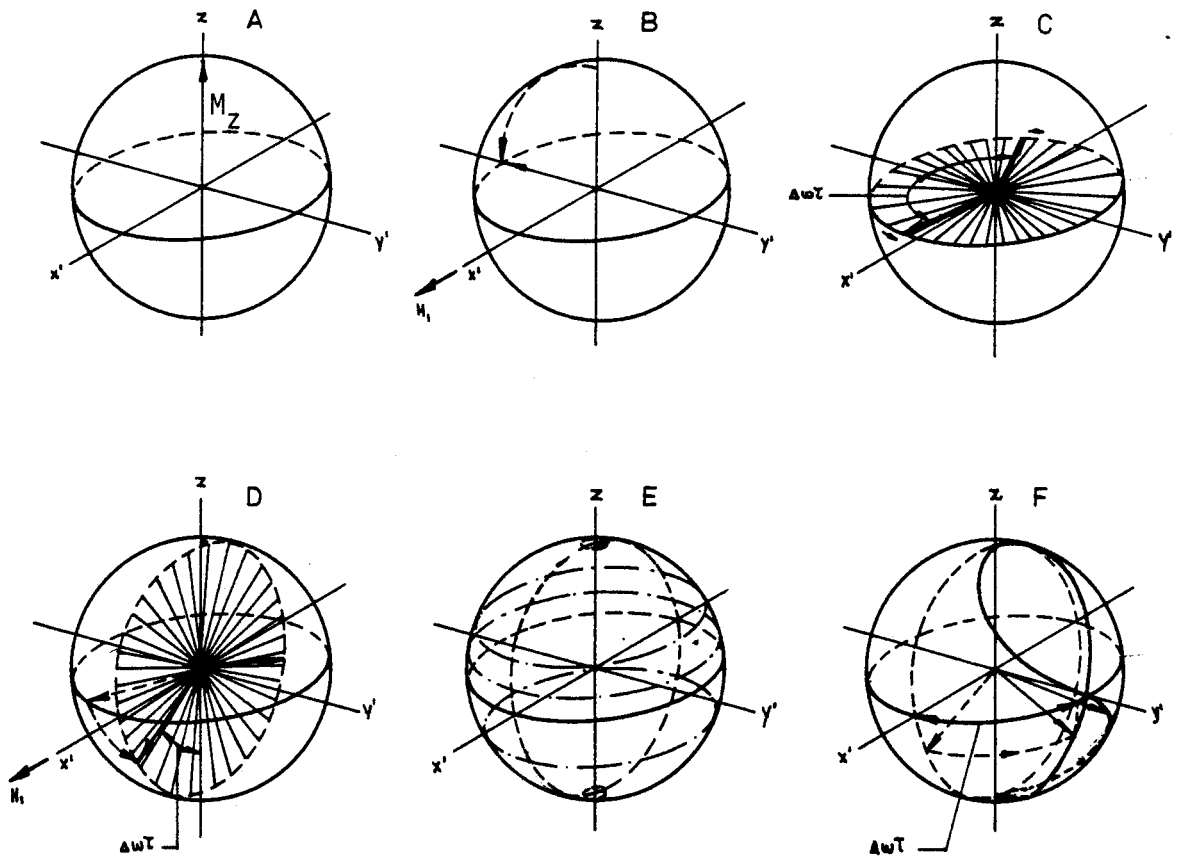

fig. 3.3.5   Formation of the spin-echo (in the rotating frame S').

vectors will have again precessed angles $\Delta\omega\tau$ respectively from their positions at t=τ so that they terminate in a figure eight patterns whose equation is $\Theta=\varphi$ (fig. 3.3.5. F).

We will now describe the formation of the spin-echo in more detail. Because the moment vectors maintain a symmetry around the y'-axis $M_x'(t)$ equals zero.

If we assume that $t_w \ll 1/(\Delta\omega)_{1/2}$, we can neglect the duration, t_w of the pulses. The initial condition $M_y'(0,\Delta\omega)$ is given by $M_y'(0,\Delta\omega) = M_z \, g(\Delta\omega)$ in this case (see fig. 3.3.5. B). Following one moment vector $M'(\Delta\omega)$ we can conclude that for $t > \tau$ the component $M_y'(t,\Delta\omega)$ is given by:

$$M_y'(t,\Delta\omega) = M_z \, g(\Delta\omega) \, \sin \Delta\omega \, \tau \, \sin \Delta\omega \, (t-\tau) \qquad 3.3.11$$

The component $M_y'(t)$ is determined by integrating over all the frequencies $\Delta\omega$:

$$M_y'(t) = \frac{M_z}{2} \left[\frac{\sin \{(\Delta\omega)_{1/2}(t-2\tau)\}}{(\Delta\omega)_{1/2}(t-2\tau)} - \frac{\sin \{(\Delta\omega)_{1/2} \, t\}}{(\Delta\omega)_{1/2} \, t} \right] \qquad 3.3.12$$

In the laboratory frame the component $M_y'(t)$ is precessing with ω_0. With aid of a coil we obtain an induction voltage $V(t)$ which is proportional to 3.3.12. According to the first term on the right side of 3.3.12. the echo maximum occurs at $t=2\tau$ and is proportional to the magnetization M_z.

Equation 3.3.12. indicates that periodic maxima should occur at times $2\pi/(\Delta\omega)_{1/2}$ sec apart. These maxima are not observed in practice because the choice of $g(\Delta\omega)$ in this simple model does not correspond to the experimental distribution.

3.3.3. General analysis of free induction decay and spin-echo (ref. 12)

In this section the results of a more general analysis of spin-echo will be given. In this analysis the Bloch equations are used and a spectrum $g(\Delta\omega)$ is chosen that approximates the actual distribution of the moment vectors. Also the relaxation times T_1 and T_2 are taken in account.

At $t=0$ the nuclear magnetization is Mz. At $t=0$ a pulse sequence of two pulses, each with a pulse width t_w and time τ (short delay) between the pulses is applied (see fig. 3.3.6.).
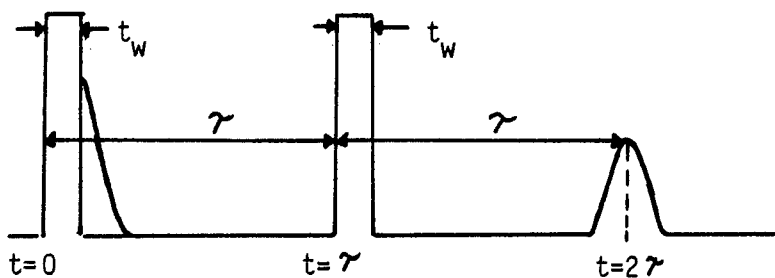

fig. 3.3.6   The pulse sequence of a double pulse.

For the determination of these solutions the following assumptions have been made:

- the decay terms are neglected during the pulses and this is only allowed as long as $t_w \ll T_1, T_2$;
- the analysis does not take in account any sort of inhomogeneity of the H_1 field;
- also the condition $\omega_1 \gg (\Delta\omega)_{1/2}$ and $\tau \gg t_w$ are imposed.

For the frequency distribution $g(\Delta\omega)$ a Gaussian distribution is choosen:

$$g(\Delta\omega) = (2\pi)^{-1/2} \, T_2^* \, exp\left[-(\Delta\omega \, T_2^*)^2/2\right],$$

$$T_2^* = (2 \ln 2)^{1/2} / (\Delta\omega)_{1/2}$$

3.3.13

where the integral of $g(\Delta\omega)$ over all $\Delta\omega$ is equal to unity.

The results of this analysis are given by (ref. 12):

(a) $t \leq \tau$

$$V(t) \sim M_z \, \sin \omega_1 t_w \, \exp\left[-\frac{t^2}{2(T_2^*)^2} - \frac{t}{T_2}\right]$$

(b) $t \geq \tau$

$$V(t) \sim M_z \, \sin \omega_1 t_w \left\{ \left(\sin^2 \frac{\omega_1 t_w}{2} \, \exp\left[-\frac{(t-2\tau)^2}{2(T_2^*)^2} - \frac{t}{T_2}\right]\right. \right. \qquad 3.3.14$$
$$\underbrace{\phantom{\left(\sin^2 \frac{\omega_1 t_w}{2} \, \exp\left[-\frac{(t-2\tau)^2}{2(T_2^*)^2} - \frac{t}{T_2}\right]\right.}}_{A}$$

$$\underbrace{- \cos^2 \frac{\omega_1 t_w}{2} \, \exp\left[-\frac{t^2}{2(T_2^*)^2} - \frac{t}{T_2}\right]\Bigg\}}_{B'}$$

$$\underbrace{- M_z(\tau) \, \sin \omega_1 t_w \, \exp\left[-\frac{(t-\tau)^2}{2(T_2^*)^2} - \frac{t-\tau}{T_2}\right]}_{B''}$$

1. The induction signal immediately following the first pulse described by eq. 3.3.14. (a) is called free induction decay. It is porportional to Mz. The decay is determined by T_2^* which is proportional to $1/(\Delta\omega)_{1/2}$ and by the relaxation time T_2. T_2^* follows from the frequency spectrum $g(\omega)$ (see eq. 3.3.13.). The spectrum of nuclei in solids, $g(\Delta\omega)$, is determined by the inhomogeneities in the local field $H_{loc.}$, due to neighbouring nuclear and electronspins and the inhomogeneities in the external field . The T_2^* was about 3-10 µsec in our experiments. In general the transverse relaxation time T_2 is determined by mutual nuclear spin-spin flipping (spin-spin relaxation), local magnetic field fluctuations at the position of the nucleus caused by neighbouring spins and paramagnetic ions ,and the nuclear spin lattice relaxation (ref. 12).
The T_2 in solids is of the order 10-100 µsec. For small T_2^* or T_2 the free induction decay is small. Because the pulse is mostly followed by an electronic "distortion" (ringing) in practice as is shown in chapter 4 &4.4., the free induction decay is difficult to observe. For this reason we do not use the method in which the recovery of Mz as function of the time is measured with the free induction decay as shown in fig. 3.2.1. (a).

2. In 3.3.14 (b) we can distinguish two terms; the first term A predicts the spin-echo with the maximum at $t=2\tau$, the second term B (B' and B") predicts a free induction decay immediately followirg the second pulse.
We first consider term A. In 3. we will consider term B.
The width of the spin-echo is proportional to T_2^* (about 3-10 µsec). The amplitude of the maximum of the spin-echo is decreasing exponentially as

a function of 2τ. The characteristic time is given by T_2. The amplitude of the spin-echo as function of 2τ is shown in fig. 3.3.7.
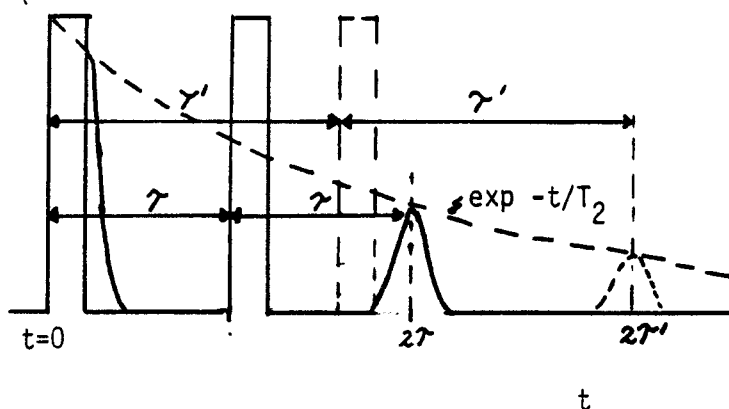

fig. 3.3.7   Spin-echo amplitude as a function of 2τ.

The maximum time at which a spin-echo can be observed is determined by the T_2. Because T_2 is short for solids (10-100 μsec), the pulse width of the pulses and the distance τ between them must be short. For obtaining small $\pi/2$-pulses the amplitude of the alternating field, H_1, must be large (for protons we need a field $H_1 \simeq 40$ Oe in order to obtain a $\pi/2$-pulse of 2 μsec). The minimum distance 2τ was about 20 μsec in our experiment. So for small T_2 (of the order of 20 μsec) we can not observe the spin-echo.

According to eq. 3.3.14. (b) the spin-echo amplitude is proportional to the pulse width t_w as follows:

$$V(t) \sim \sin \omega_1 t_w \sin^2 \frac{\omega_1 t_w}{2} \qquad 3.3.15$$

This relation is shown in fig. 3.3.8.

From fig. 3.3.8. it appears that we observe a maximum spin-echo when we give two pulses with $\theta = \omega_1 t_w = 2/3\pi$.

3. The free induction decay following the second pulse is determined by the terms B' and B'' of the eq. 3.3.14. (b). The term B' is proportional to   a same decay term (exp $[-t^2/2(T_2^*)^2 - t/T_2]$) as the free induction decay following the first pulse. If we apply the second pulse at time τ at which the free induction decay following the first pulse is zero, the term B' is zero.
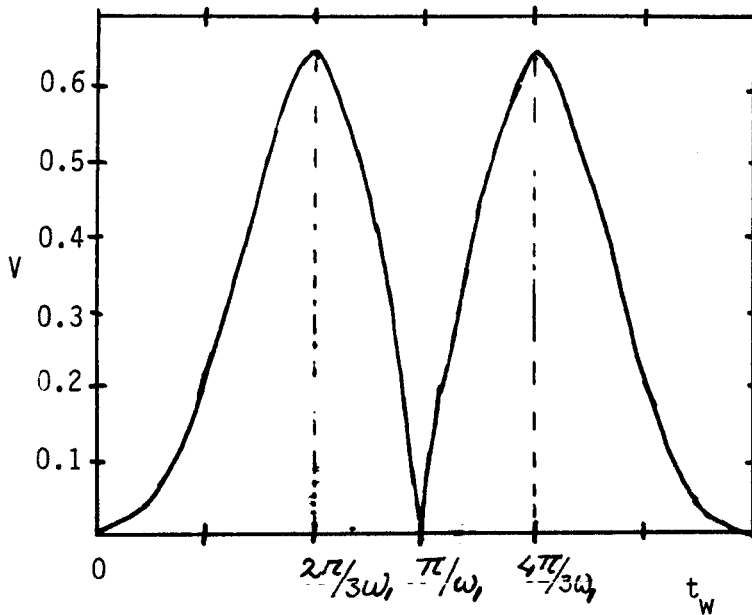
fig. 3.3.8   Spin-echo amplitude as a function of the pulsewidth.

The B'' term is proportional to Mz(τ), the magnetization along the
z-axis when the second pulse is applied. Mz(τ) is only different from
zero in two cases. First if τ is of the same order as the nuclear
spin lattice relaxation time, there is a recovery of the magnetization
to the z-axis. Secondly, if we do not apply $\pi/2$-pulses, there will be
a component of the magnetization along the z-axis after the first
pulse.

In cases that we apply $\pi/2$-pulses and $\tau \ll T_1$ the magnetization Mz(τ)
will be zero which means that the term B'' will also be zero.

Chapter 4 Experimental set-up

4.1. Introduction

In chapter 3 we have described an experimental method to measure the T_1. In this section the experimental apparatus will be considered. In &3.2 we introduced already the pulsed resonance technique in which a coil is used to apply an alternating field H_1 to a sample and to pick up an induction signal generated by the sample. This technique is employed in the experimental set-up which we constructed to measure the nuclear spin lattice relaxation time. The experimental equipment can be distinguished in four main parts (see figure 4.1.1):

(a) pulse generator, for comb and double pulse modulation (&4.2)
(b) r.f. generator, to apply an oscillating voltage to the coil (&4.3)
(c) the insert including the sample holder (&4.4)
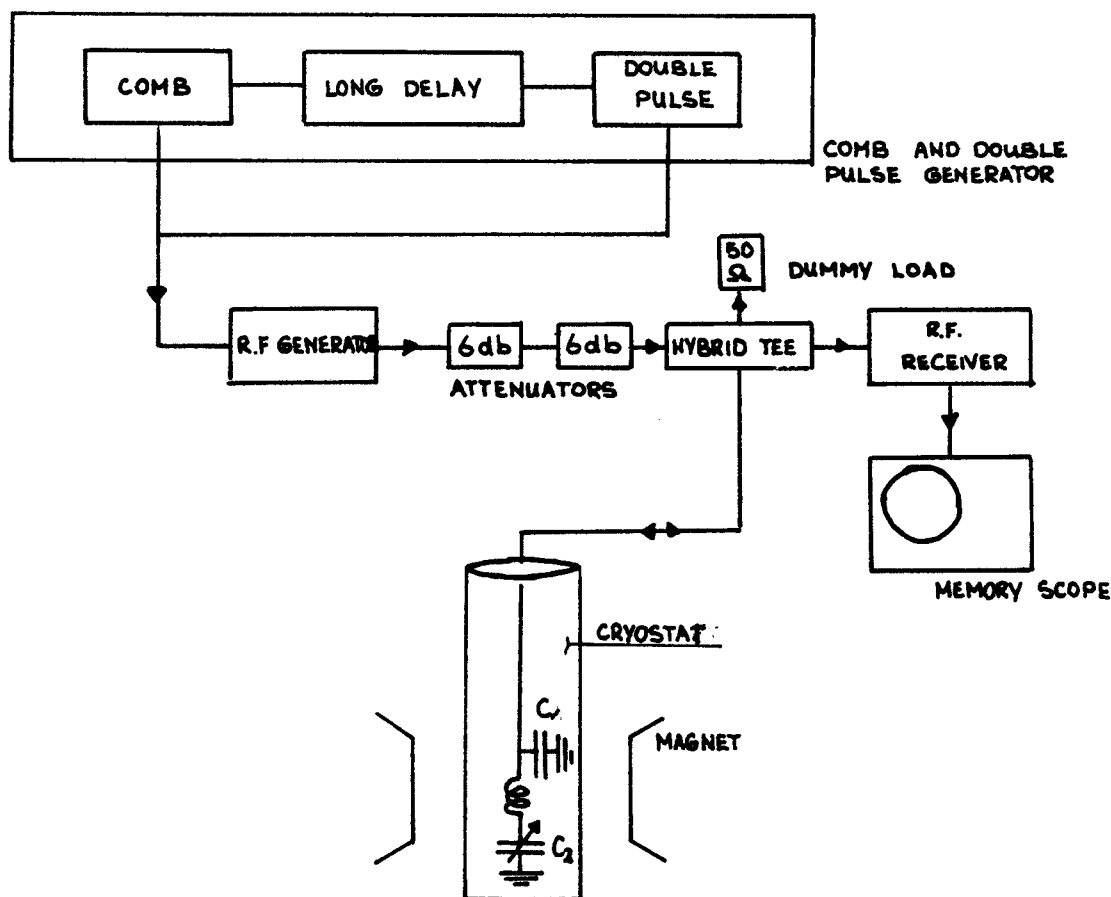(d) r.f. receiver, to detect an induction signal (&4.5)

fig. 4.1.1   Schematic view of the experimental set-up.

4.2. Pulse generator for comb and double pulse modulation

In &3.2 we introduced an experimental method to measure T_1 in which
we applied a pulse sequence consisting of a comb and a double pulse,
the various pulses being the envelope of a r.f. carrier of frequency
ω_0. The pulse-modulated r.f. field was supplied by a r.f. generator
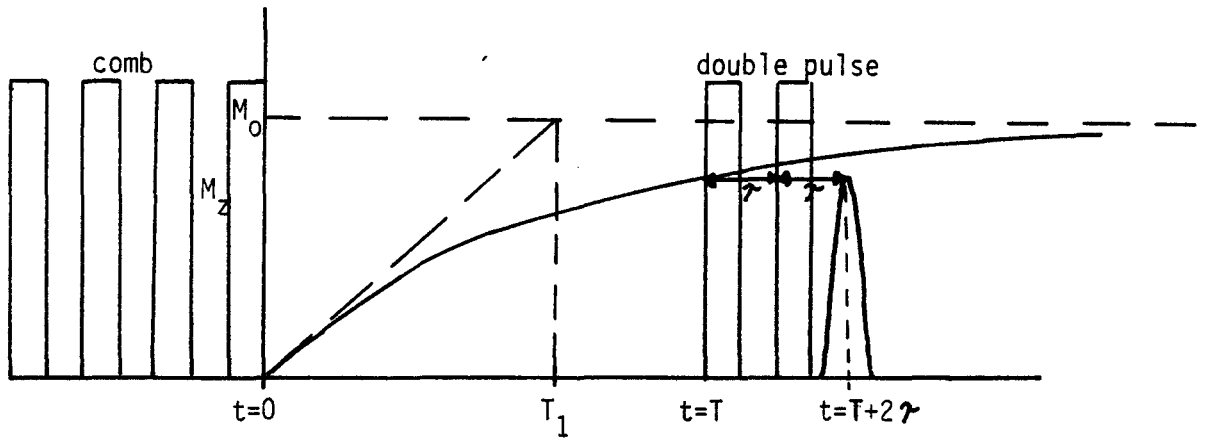which will be treated in the next section.

fig. 4.2.1   Experimental method to measure the recovery of M_z
as a function of t.

For the pulse modulation of the r.f. carrier we use an external pulse
modulation programmer. In fig. 4.2.2. a schematic view of this programmer
is shown.

With this unit three different pulse modulation sequences can be applied
to the r.f. generator. The comb or double pulse sequence can be used
separately or they can be used in combination, as is shown in fig. 4.2.2.
The number of pulses in the comb can be set equal to 1, 2, 4, 8, 10 or 20.
The distance between the pulses in the comb is determined by an audio
frequency sine-wave. The highest frequency of this generator amounts
to 250 kHz, which corresponds to   a distance of 4 μsec between the
leading edges of adjacent pulses. The pulse width of the pulses in the
comb can be varied continuously from about 1 to 5 μsec. The width of the
pulses of the double pulse can also be varied from about 1 to 5 μsec.
The short delay τ between these two pulses can be varied from 10 to
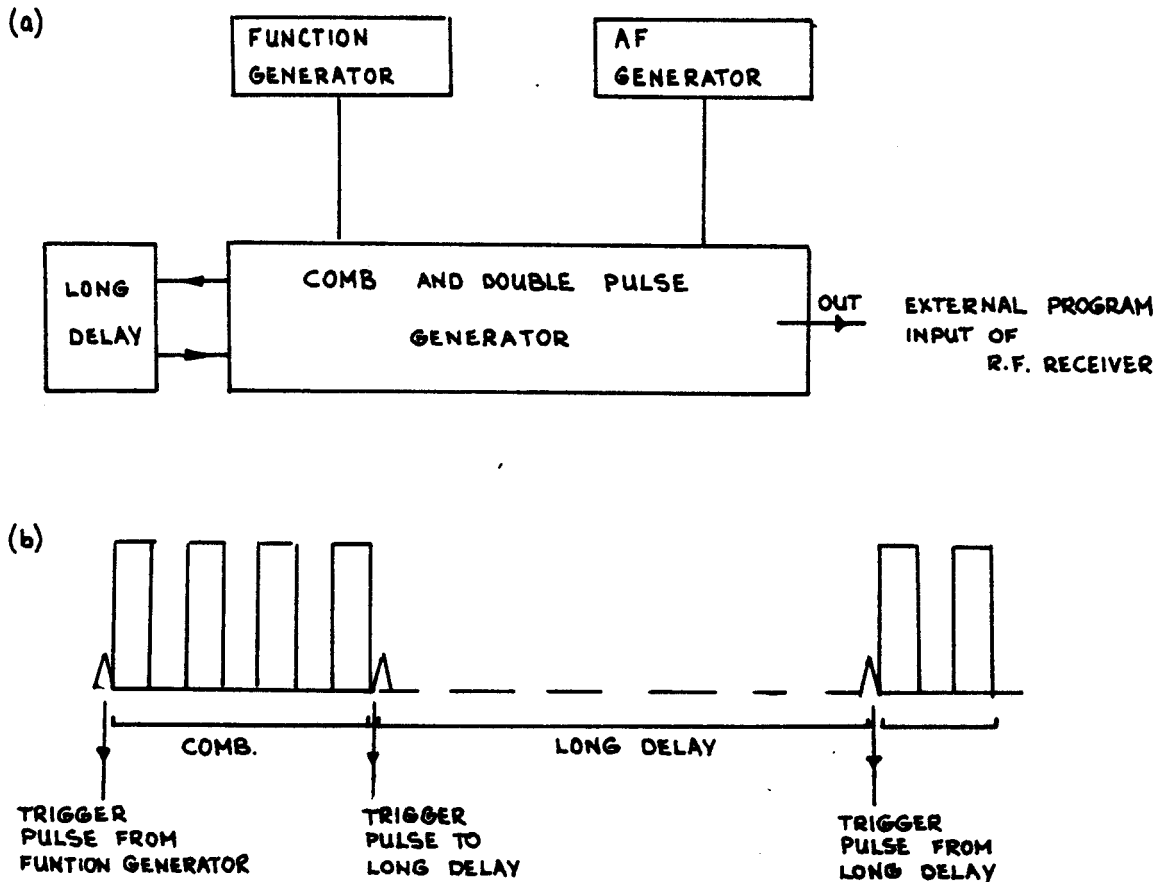
(a)

(b)

fig 4.2.2   (a)   Schematic view of the comb and double pulse generator

           (b)   A typical generated sequence. For the explanation
of the various parts, see text.

1000 μsec.

The long delay between the comb and double pulse is adjusted by the delay
trigger of an oscilloscope (Tektronix type 547) and can be varied from
0.1 μsec to 50 sec.

The generator can operate in a single shot mode with a manual triggering
or a repeated mode, in which the repetition rate is determined by a
function generator giving a square wave output.

If very high repetition rates of the comb and double pulse sequence are
used, the duty cycle of the r.f. generator must be considered. Up to a
duty cycle of 0.1% the amplitude of the r.f. carrier is constant. If,
for instance, the pulses of the comb (maximum 20) and of the double
pulse are about 5 μsec wide, a repetition rate of about 10 Hz is possible
without a significant decrease of the output power of the r.f. generator.

4.3. r.f. Generator

In our actual experimental set-up the r.f. generator and r.f. receiver
are combined in one commercial apparatus (Matec, model 6600). In this
section we will describe the most important characteristics of the
r.f. generator. The r.f. source, in fact, consists of a pulsed oscilla-
tor. This oscillator delivers up to 1 kW peak power in a 50Ω load. The
oscillator is switched off and on by a modulation program. Several
internal modulation programs are incorporated in the Matec such as a
single and a double pulse sequence. As already mentioned, above, a
more versatile external programmer is used (see &4.2).
The r.f. generator can be used in a wide frequency range because several
plug-in units are available which operate in a frequency range 10-90 MHz,
90-300 MHz and 300-700 MHz, respectively, Both the r.f. generators and
the r.f. receiver must be tuned to the desired frequency. This frequency
follows form the resonance condition $\omega_0 = \gamma H_0$ of the experiment (H_0 is
the magnetic field at the position of the nucleus and γ is the gyro-
magnetic ratio). The tuning procedure for the r.f. generator is described
in appendix A. Tuning data supplied by the manufacturer are available.
Although these are not so extensive, they can be used for a coarse tuning
of the generator.
As the r.f. pulses have a final width, the r.f. pulse is not monochromatic,
but consists of a frequency spectrum as is described in appendix C.
For further details, such as duty cycle limits and long pulse operation
the reader is referred to the manual of the Matec (ref. 14).

4.4. The insert including the sample holder

The output power of the r.f. generator is coupled to an LC-circuit via
two 6 db attenuators and a hybrid Tee, as is schematically shown in fig.
4.4.1.
The attenuators are used for two reasons. First they protect the hybrid
Tee against the high output voltage swing of the r.f. generator (630 volts
peak to peak) and secondly, they prevent the frequency of the pulse
oscillator to be pulled away from the calibrated data, which occurs when
the output is not terminated with 50Ω. The input impedance of the attenuators
is about 50Ω even when they are not exactly terminated with 50Ω.
A hybrid Tee is used to isolate the generator output and receiver input,
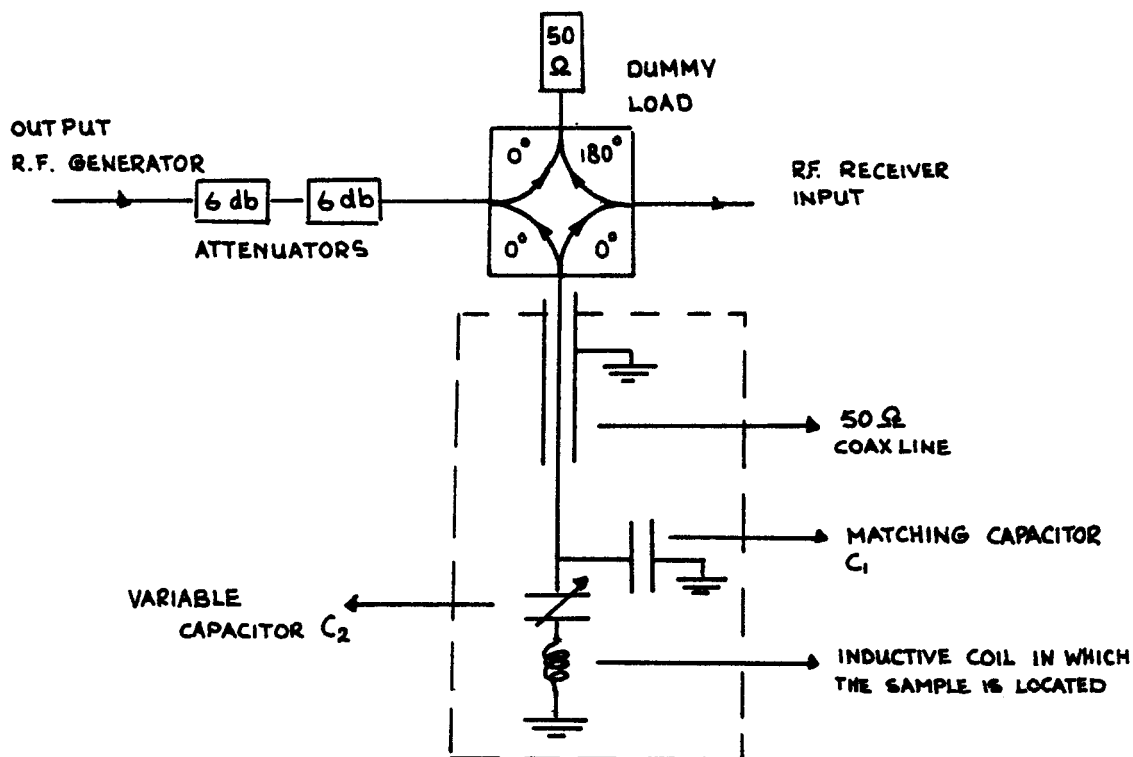from each other (40 db) over a wide range of frequencies, in this way

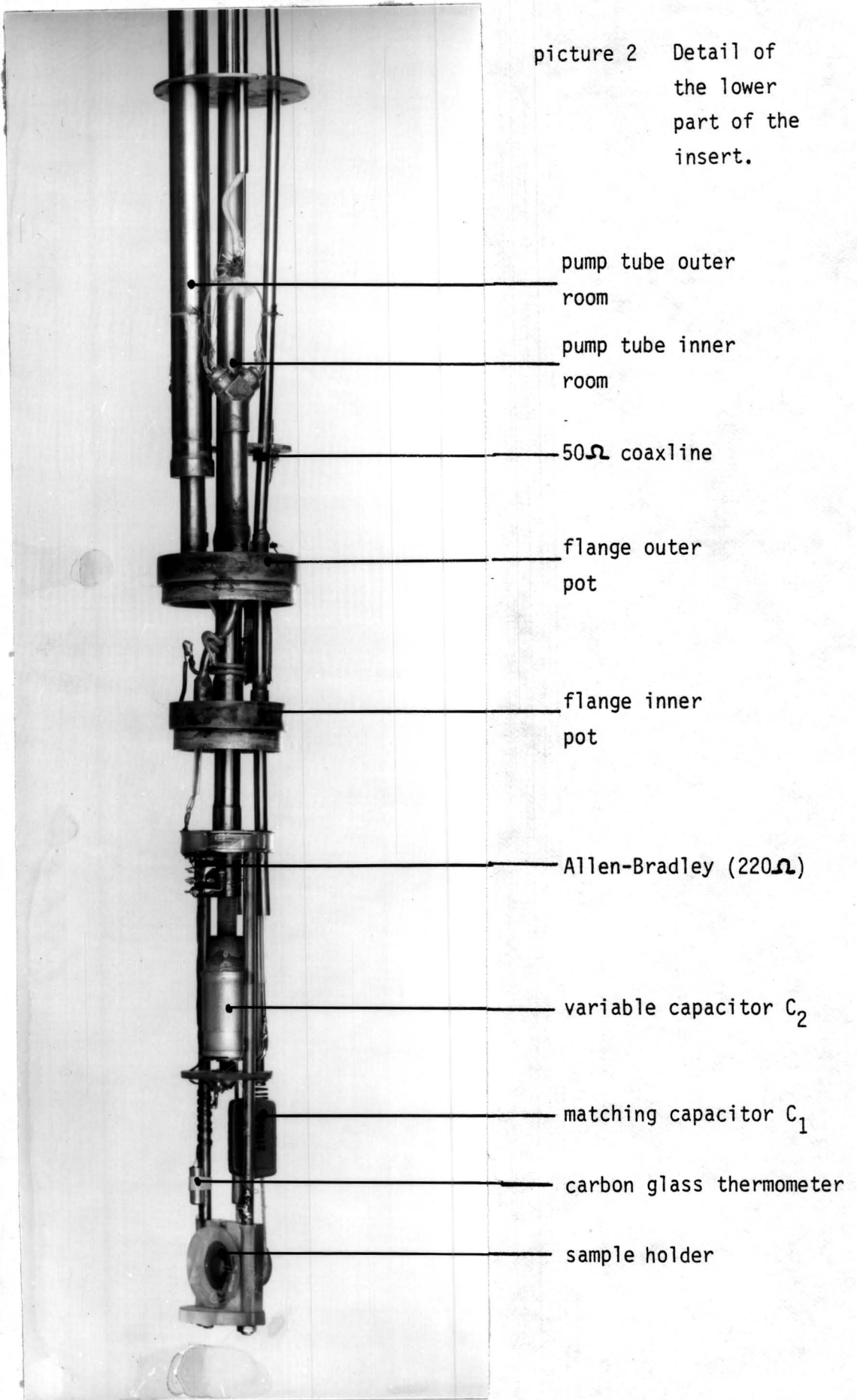fig. 4.4.1   Schematic r.f. circuit used in the relaxation time measurements.

good impedance matching of the total circuit can be achieved while the overload of the receiver is reduced.

The lower part of the insert is shown on picture 2. In this part the sample, the LC-circuit and the capacitor to match the characteristic impedance of the coaxial line to the LC-circuit are located. The coil with the sample is not present on this picture, but it is normally fixed on the sample holder. This sample holder can be rotated around an horizontal axis. This rotation can be controlled at the top of the insert. In fig. 4.4.2. the electronic circuit of the insert and an equivalent circuit are shown.

C_2 is a cylindric, variable capacitor (0-65 pF) of which the capacity can be changed at the top of the insert via a long stainless steel tube (picture 2). C_1 is a fixed capacitor which is used for matching the impedance of the 50Ω coaxline to the LC-circuit. The impedance of the LC-circuit is given by:

$$Z_1 = R + j \frac{(\omega^2 L C_2 - 1)}{\omega C_2} \qquad 4.4.1$$

picture 2   Detail of
             the lower
             part of the
             insert.

pump tube outer room

pump tube inner room

50 Ω coaxline

flange outer pot

flange inner pot

Allen-Bradley (220 Ω)

variable capacitor C_2

matching capacitor C_1

carbon glass thermometer
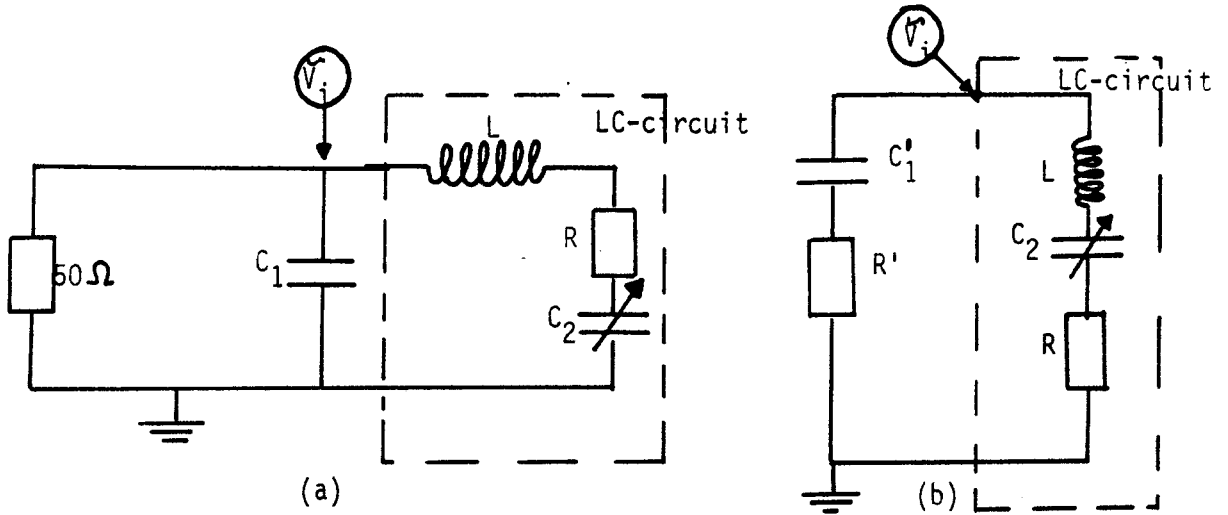
sample holder

fig. 4.4.2   (a) The actual electronic circuit of the insert.
            (b) An equivalent circuit.

The resistance R is mainly determined by the losses within the coil. If
the frequency of an oscillating voltage across this LC-circuit is equal
$1/\sqrt{LC_2}$ the impedance is equal to R. To obtain maximum power transfer
from the 50Ω coaxline to the LC-circuit and vice versa the impedance
of the line must be matched to the resistance R (LC-circuit in resonance).
For this purpose we use the capacitor C_1. The impedance of the coaxline
in parallel with this capacitor is given by:

$$Z_2 = \frac{50}{1+\omega^2 C_1^2 \, 50^2} \; - j\left(\frac{\omega C_1 \, 50}{1+\omega^2 C_1^2 50^2} \, 50^2\right) \qquad 4.4.2$$

The coaxline is well matched to the LC-circuit if the real and imaginary
parts of Z_1 and Z_2 are equal to each other:

$$(a) \qquad \frac{50}{1+\omega^2 C_1^2 50^2} = R$$

$$(b) \qquad \frac{\omega \, 50 \, C_1}{1+\omega^2 C_1^2 50^2} = \frac{1-\omega^2 L C_2}{\omega C_2} \qquad 4.4.3$$

If ω and R are known (ω is determined by the resonance condition $\omega_0 = \gamma H_0$)
we can calculate the value of the matching capacitor C_1 from eq.4.4.3 (a).
In order to satisfy eq. 4.4.3. (b) we have to change the capacity C_2 from
the original value, corresponding to series resonance of the isolated
LC-circuit (eq. 4.4.1.). Obviously, the capacity of the LC-circuit is not

determined by C_2 alone but also by C_1', (see fig. 4.4.2 (b)):

$$C_1' = \frac{1 + \omega^2 C_1^2 (50)^2}{\omega^2 C_1 \, 50}$$

4.4.4

The resonance frequency of the circuit is now given by:

$$\omega_m = \sqrt{\frac{1}{C_1' C_2 / C_1' + C_2}}$$

4.4.5

The equivalent circuit at resonances is shown in fig. 4.4.3.
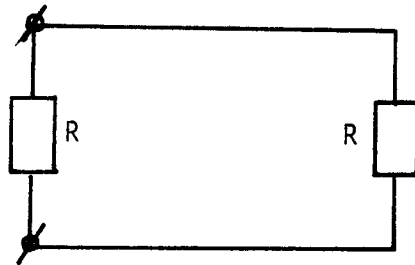

fig. 4.4.3   The equivalent circuit of the r.f. section of the insert at resonance.

As we actually use a fixed capacitor C_1 we achieve only perfect impedance matching for one frequency ω_m. At other frequencies a part of the r.f. signal is reflected as is shown in fig. 4.4.4. (a).
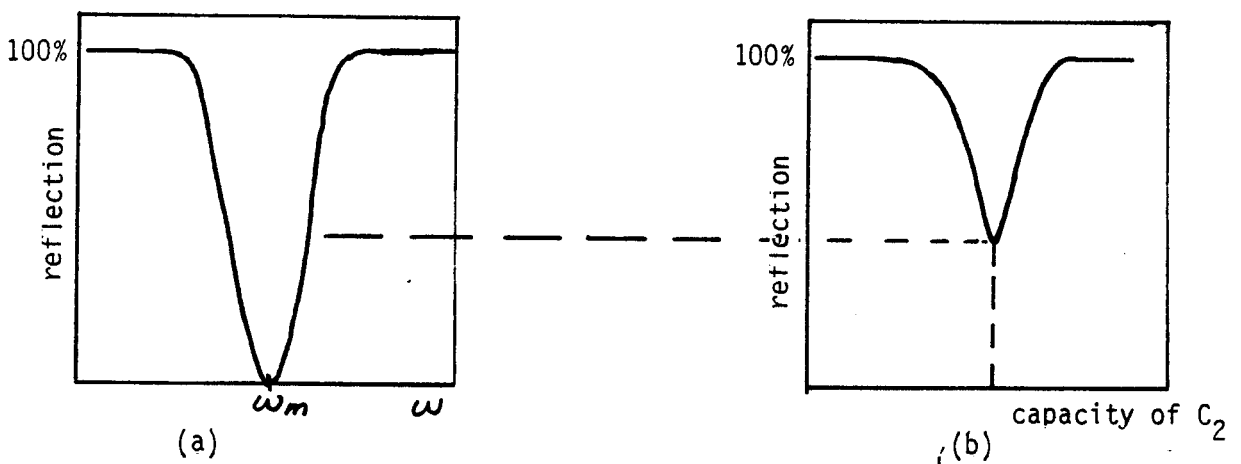

(a)

(b)

fig. 4.4.4   (a) Reflection of the r.f. signal as a function of ω
(For each value of ω , C_2 is adjusted to maintain se-
ries resonance of the circuit).

(b) Typical reflection of r.f. signal for one fixed frequency
ω as a function of the variable capacitor C_2. (ω near ω_m).

In practice it appears that we are able to measure in a wide frequency range around ω_m. This range is mostly determined by the variable capacitor C_2. In case of ω_m about 40 Mhz, we could measure from 30 to 50 Mhz. Because we do not know in advance the exact value of the resistance R at - for instance - liquid ^{4}He temperatures we cannot calculate the exact value of the capacitor C_1. In general eq. 4.4.3. is used as a first estimate and C_1 values which give satisfactory results are determined experimentally. The actual value of C_1 is found to be not critical,in fact, changes of about 25% do not significantly degrade the performance of the circuit.

In principle, perfect impedance matching has two advantages: first the r.f. power is fully transferred to the insert and secondly, the induction signals (spin-echo) are fully transferred to the receiver. However, in the actual experiments, a perfect matching has serious disadvantages, as will discussed below.

Because the resistance R is very small (about 3Ω) the unloaded Q-factor of the LC-circuit ($Q_{LC} = \frac{\omega L}{R}$) is generally very high. At the frequency ω_m for which the impedance matching is perfect, the Q-factor of the insert (the loaded Q) is equal to $1/2Q_{LC}$ as can easily be seen from fig. 4.4.3. This loaded Q-factor of the insert therefore is also high and the r.f. pulses appear to be followed by a remarkable "ringing" of the circuit as is shown in fig. 4.4.5.
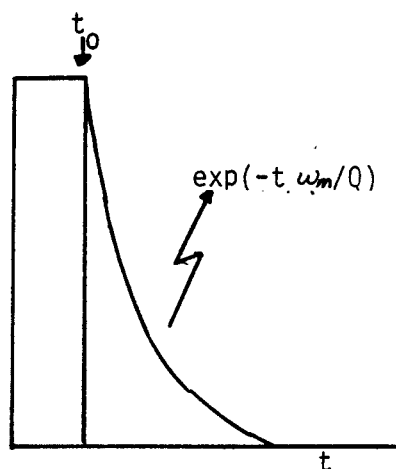

fig. 4.4.5 If we switch off the r.f power at t_o the voltage across the LC circuit drops exponentially to zero ("ringing").

Because in general the spin-echo signal has a small amplitude, it is readily obscured by the "tail" of the second r.f. pulse. For large values of T_2 the distance between the two r.f. pulses (short delay τ) can be made long enough to obtain a spin-echo (at 2τ) which is resolved from the tail of the second r.f. pulse. For small values of T_2 this is not possible and in this case it is disadvantageous to have a large loaded Q-factor.

In that case it appears to be advantegeous to measure at a frequency ω that differs from ω_m (see fig. 4.4.4. (b)). In this case the loaded Q is smaller and the tail of the r.f. pulse is also smaller (proportional to Q/ω).

4.5. r.f. Receiver

The insert is connected with the r.f. receiver via the hybrid Tee. We use the Matec r.f. receiver. The receiver of each available plug-in unit covers the same frequency range as the corresponding r.f. generator i.e., 10-90 MHz, 90-300 MHz and 300-700 MHz, respectively. In the actual experimental set-up the plug-unit for 10-90 MHz is used. The minimum observable signal of this receiver is 4 μV and the bandwidth is about 1,5 MHz according the specifications. Both these characteristics have been checked.

The tuning of the r.f. receiver is described in appendix A. The output of the r.f. receiver (video out) corresponds to the envelope of the r.f. induction signal obtained from the insert. This output may be coupled to an oscilloscope and/or electronic devices such as a sample and hold circuit. A prototype of a. sample and hold circuit has recently been constructed and tested.

In &4.1. to &4.5. we have described the main parts of the apparatus. In the last section (&4.6) of this chapter we will describe the temperature regulation and thermometry of the insert.

4.6. Temperature regulation and thermometry

With the experimental set-up described in &4.4 we are able to measure T_1 at roomtemperature. Because we are in general interested in the temperature dependence of T_1, it is necessary to have a possibility to regulate the temperature of the sample.

When the insert is located in a cryostat filled with liquid helium or nitrogen T_1 can be measured at T = 4.22 K and T = 77 K, respectively. By pumping the helium or nitrogen bath the temperature can be regulated from 1.1 K < T < 4.22 K and 67 K < T < 77 K, respectively. When we want to measure T_1 at temperatures above T = 77 K and temperatures in the intermediate temperature region 4.22 K < T < 67 K it is necessary to solder two pots to the lower part of the insert (see picture 3).
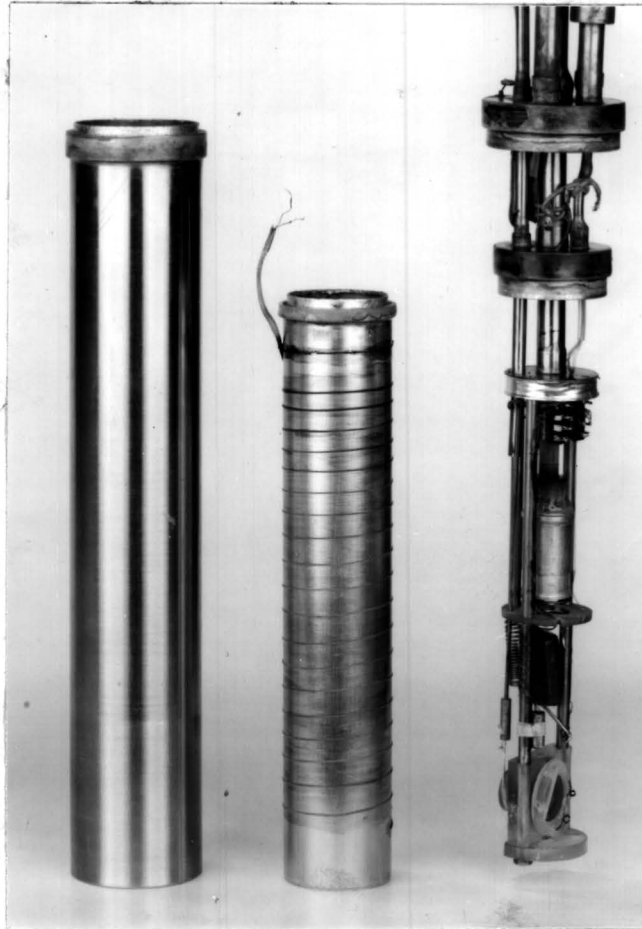
picture 3 Two pots (the left is the outer pot, the right is the inner
pot) together with the lower part of the insert.

These two pots are soldered with tin on the two flanges of the insert. In
the edges of these flanges thermocoax is put (on picture 3, a small part
of it is just visible at the upper flange) which we use to heat the flanges
for soldering. For the inner pot a current of about 2.5 A through this
thermocoax is sufficient to solder it, for the outer pot a current of
about 2A is sufficient. This method of soldering appears to work very
well. The tubes through which the supply wires of the thermometers and
the heater are conducted to the sample room are connected with the flanges
and for this reason will also become hot during the soldering. So one
has to be very carefull with heating the flanges because it is possible
that these wires are damaged when the flanges become too hot. Both rooms,
that of the inner and the outer pot are connected via small tubes to the top
of the insert. The tubes are connected to a pumping system which consists
of a diffusion pump and a rotary pump.
The inner pot is made of copper. On the outside of this pot we wound
manganine wire (total resistance is about 188Ω). The copper pot with

the manganine wire functions as a heater.

We shall now describe the temperature regulation of the sample. The inner pot is filled with ^{4}He contact gas and the outer pot is pumped vacuüm (10^{-5}). Because the inner pot is connected with the bath by tubes that lead through the two flanges the ^{4}He contactgas and therefore the sample is cooled. The cold input is determined by the bath temperature and the pressure in the outer pot. When we do not use the heater the sample will have approximately the same temperature as the bath. When we apply a voltage over the manganine wire the inner pot is heated. This leads to an heat input to the sample through the ^{4}He contact gas. The final temperature of the sample is determined by the ratio of the cold- and heat input. By regulating the heat input we could vary the temperature from 4.3 K to 80 K using a liquid helium bath. In a nitrogen bath we reached a maximum temperature of about 160 K.
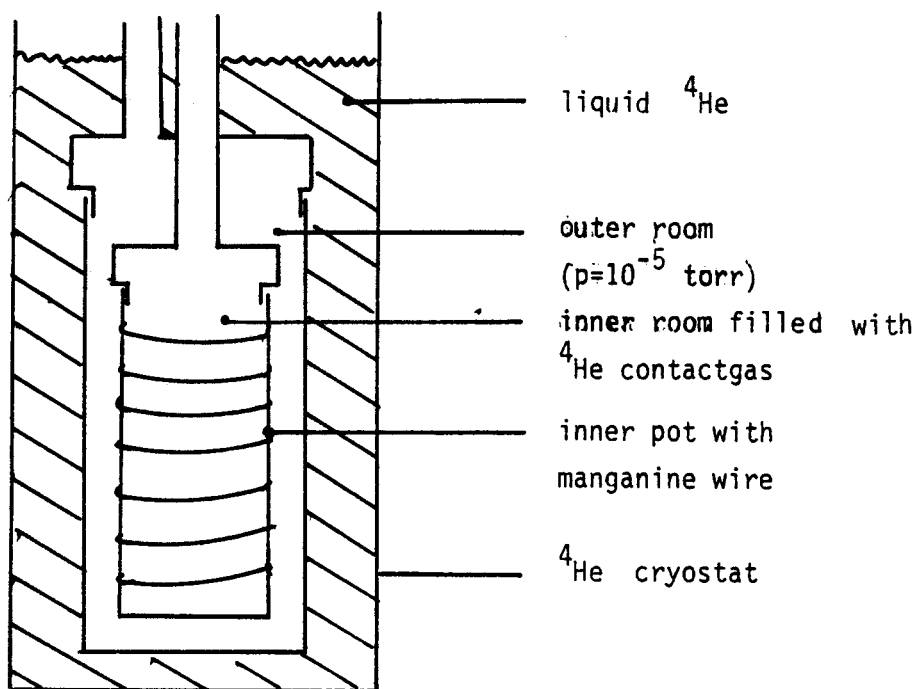

fig. 4.6.1   Insert with the two pots in ^{4}He bath.

For the temperature regulation of the sample we have located an Allen-Bradley resistance (220Ω at roomtemperature) in the inner pot. At low temperatures the Allen-Bradley has a large temperature dependence. The resistance decreases with the temperature. The Allen-Bradley is connected

with a three wire resistance bridge (ref. 15). The output of the lock-
in amplifier of this bridge is connected via a booster amplifier to the
heater. This booster amplifier only gives an output signal when the output
signal of the lock-in is negative. This means that if the Allen-Bradley
resistance is larger than the resistance of the bridge the inner pot is heated.
In this case there is via the ^{4}He contactgas a .heat input to the Allen-
Bradley. The difference of the resistance of the Allen-Bradley and the
resistance of the bridge stabilizes if the heat input via the ^{4}He con-
tactgas to the Allen-Bradley equals the cold input to it. For more
details about the three wire resistance bridge and the heating system the
reader is referred to the literature (ref. 15).

The temperature of the sample is determined with a carbonglass thermo-
meter (type C CGR 1-2000 No. 734). This thermometer is located close to
the place where the sample is located. The ^{4}He contactgas heats the
sample and the thermometer. We assume that the temperature of the thermo-
meter is the same as the temperature of the sample.

The carbon-glass thermometer is calibrated in the range $1.5\,K < T < 293\,K$. At
low temperatures the inaccuracy is about 0.1%. Above 77 K an interpolation
to roomtemperature is used and therefore this calibration is less accurate.
The inaccuracy is about 5% in temperatures above 77 K. The carbon-glass
thermometer has a small field dependence for which we can correct (ref 16).
The carbon-glass thermometer has four output wires as is shown in fig. 4.6.2.
The contacts put on the intrinsic material have a transition resistance
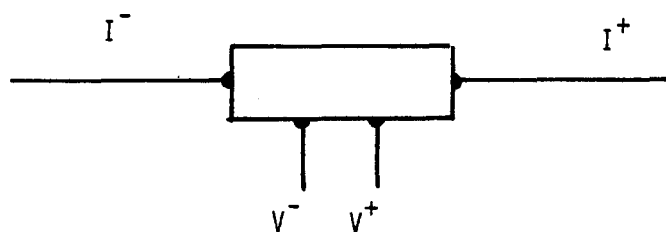which is time dependent.

fig. 4.6.2 Schematic view of a
carbon glass
thermometer

The resitance of the supply wires is large, as they are made of manganine
wire to obtain a very small heat conduction. For determining the resistance
of the carbon-glass thermometer with great accuracy in spite of the upper
facts, we use a four wire resistance bridge. With this bridge the V^+
and V^- are measured current free and so the influence of the supply wires
and the time dependent contact resistances is eliminated. This four wire
resistance bridge is described in the literature (ref. 15).

Chapter 5   Test measurements on paraffin

5.1. Introduction

In the former chapters (3 and 4) we described the experimental method and the apparatus. In this chapter we will present the results of experiments on paraffin. Because paraffin is a diamagnet, the resonance frequency of the protons is only determined by the external field. The resonance condition is given by the relation $\omega_0 = \gamma H_0$, where $\gamma/2\pi$ is 42.577 Mhz/T. We did these experiments because we wanted to test the experimental set-up we built for measuring T_1.
For two reasons we thought paraffin to be a suitable sample. First the proton resonance can be observed at roomtemperature. Secondly the spin-echo signals and the T_1 of protons in paraffin were reported by Hahn. This gave us the possiblility to compare our results with the results of Hahn.
After a short report on the preparation of the sample in section 5.2, we will discuss some specific experiments including the influence of the pulse width t_w, the time τ between the $\pi/2$-pulses and the inhomogeneity of the external field on the shape and the height of the observed spin-echo in section 5.3. In section 5.4. the actual measurement of T_1 will be treated. Section 5.5. will be devoted to a discussion of some sources of inaccuracies which were encountered during the measurements. The conclusions are formulated in section 5.6.

5.2. Preparation

In this section we will give a short report on the preparation of the sample of paraffin.
By melting paraffin and putting it in a cylindric form we made a cylindric sample of paraffin. Around this sample we wound isolated copperwire of 0.3 mm thick in order to obtain a coil for the LC-circuit.
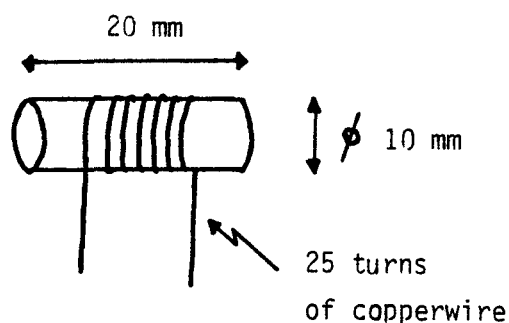

20 mm

ϕ 10 mm

25 turns
of copperwire

fig. 5.2.1. Cylindric sample
of paraffin.

For our measurements we used a coil of 25 turns of copperwire and an impedance matching capacitor C_1 of 500 pF(mica).

It appeared that in this configuration we could measure spin-echo signals in a frequency range of $15 < \nu$ (in MHz) < 25.

In the next section we will give the results of several experiments on paraffin. All experiments are performed at a resonance frequency $\nu = 19$ Mhz ($H = 4.46$ kOe).

5.3. Spin-echo experiments on paraffin

In this section we will study the influence of the pulse width, t_w, the time between the $\pi/2$-pulses, τ, and the inhomogeneity of the external field on the shape and the height of the observed spin-echo.

For convenience we recall the general equation for the induction signals following the first and the second pulse of the spin-echo experiment (see chapter 3, section 3.3.3.):

(a) $t \leq \tau$

$$V(t) \sim M_z \sin \omega_1 t_w \exp\left[-\frac{t^2}{2(T_2^*)^2} - \frac{t}{T_2}\right]$$

5.3.1

(b) $t \geq \tau$

$$V(t) \sim M_z \sin \omega_1 t_w \left\{ \underbrace{(\sin^2 \frac{\omega_1 t_w}{2}) \exp\left[-\frac{(t-2\tau)^2}{2(T_2^*)^2} - \frac{t}{T_2}\right]}_{A} \right.$$

$$\underbrace{-(\cos^2 \frac{\omega_1 t_w}{2}) \exp\left[-\frac{t^2}{2(T_2^*)^2} - \frac{t}{T_2}\right]}_{B'} \left. \right\}$$

$$\underbrace{- M_z(\tau) \sin \omega_1 t_w \exp\left[-\frac{(t-\tau)^2}{2(T_2^*)^2} - \frac{(t-\tau)}{T_2}\right]}_{B''}$$

A. Influence of the pulse width, t_w, on the height of the spin-echo

We see from eq. 5.3.1. (term A) that the height of spin-echo depends on the pulse width, t_w, according to the following relation:

$$V(t) \sim \sin \omega_1 t_w \, \sin^2 \frac{\omega_1 t_w}{2}$$

5.3.2

The frequency ω_1 is determined by the amplitude of the alternating field according $\omega_1 = \gamma H_1$. ($\gamma/2\pi = 42.577$ Mhz/T).

We measured the height of the spin-echo as function of the pulse width t_w, of which the result is shown in fig. 5.3.1.
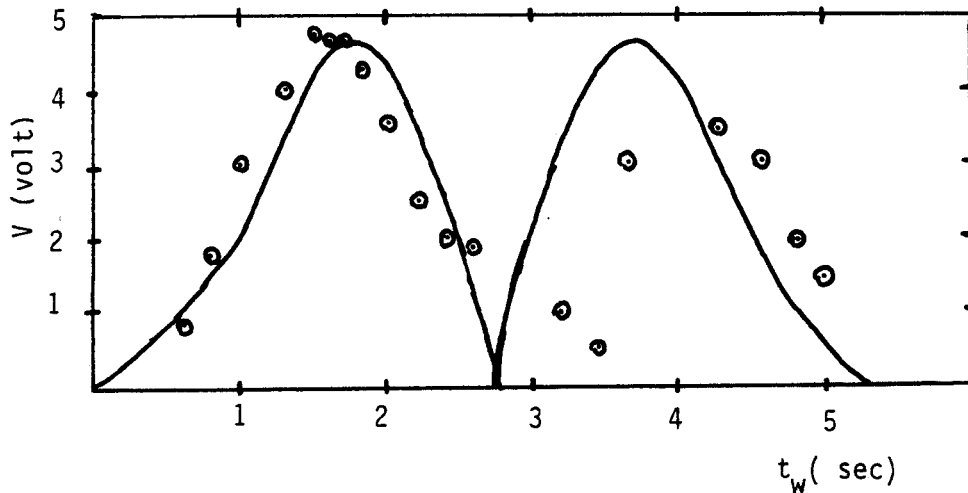

fig. 5.3.1.   The height of the spin-echo of paraffin as a function
of the pulse width t_w.

$$\underline{\hspace{3cm}} \quad V(t) = 7.2 \cdot \sin \frac{\pi\,t_w}{2.8}\ \sin^2 \frac{\pi\,t_w}{5.6}$$

We fitted the experimental result with the relation given in eq. 5.3.2. The result is represented by the solid line in fig. 5.3.1. From this figure we can draw the conclusion that the observed influence of the pulse width to the height of the spin-echo is in accordance with the prediction of the theory of Hahn.

B. Influence of inhomogeneity of the magnetic field on the width of the spin-echo

In the general analysis of spin-echo (section 3.3.3.) a gaussian frequency distribution $g(\Delta\omega)$ of the magnetic moment vectors was used. In paraffin this distribution is caused by the inhomogeneity of the external magnetic field. This inhomogeneity determines the halfwidth $(\Delta\omega)_{1/2}$ of the frequency spectrum. Because T_2 is proportional to $1/(\Delta\omega)_{1/2}$, the width of the echo is determined by the inhomogeneity of the magnetic field. If we make the field more inhomogenious the width of the spin-echo ($\exp-\frac{1}{2}(\frac{t-2\tau}{T_2^*})^2$)

becomes smaller.

We have checked this by removing the sample from the homogenious centre of the magnet to a position where the field is inhomogenious. The result is shown on picture 4, which is taken from the screen of a memory scope. The scope is triggered at the start of the double pulse and therefore the double pulse is also visible on the screen. The spin-echo in a homogenious and inhomogenious field were photographed on the same picture. Although we have not made a qualitative calculation, we can conclude from picture 4 that the width of the spin-echo is smaller in a more inhomogenious field which is in accordance with the theory of Hahn. On picture 4 we see the double pulse only for the homogenious field because we covered the double pulse when we photographed the echo in the inhomogenious field. The free induction decay which is following the first pulse is also clearly visible on this picture. Because the free induction decay is proportional to $\exp -t^2/2T_2^{*2}$ it becomes smaller in a inhomogenious field (not visible on the picture).
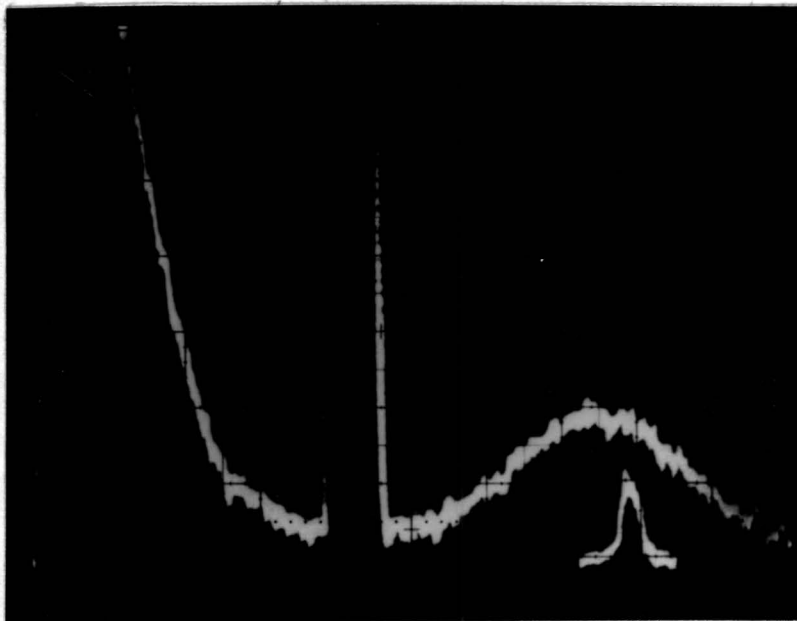
picture 4   Spin-echo in a homogenious field (broad echo) and in a inhomogenious field (small echo). Total horizontal scale 100 μsec; total vertical scale 8 volt.

C. Free induction decay following the second pulse

The free induction decay following the second pulse is determined by terms
B' and B" of eq. 5.3.1. Because we apply the second pulse at $t=\tau$ at
which the free induction decay after the first pulse is zero ($\exp[-\tau/2(T_2^*)^2-\tau/T_2] \approx 0$), the term B' will be zero.

The magnetization $Mz(\tau)$ in term B" will be different from zero in two cases.
First if τ is of the same order as T_1, the recovery of the magnetization
along the z-axis will contribute to $Mz(\tau)$. Secondly if we do not apply
$\pi/2$-pulses, we obtain a magnetization along the z-axis after the first pulse.
Because $\tau(15-40 \ \mu sec)$ is much shorter than $T_1(57 \ msec)$ for paraffin, $Mz(\tau)$
is determined by the width of the pulses. If we do not apply $\pi/2$-pulses, $Mz(\tau)$
differs from zero and we obtain a free induction decay following the second
pulse.

In the case of picture 4 the pulse width, t_w, of the two pulses was adjusted
until the free induction decay after the second pulse was zero (we applied
$\pi/2$-pulses).

Picture 5 is taken in the case that the pulsewidth, t_w, was smaller than
that in the case of picture 4 (we applied θ-pulses with $\theta < \pi/2$). On picture
5 the free induction signal after the second pulse is observed clearly.
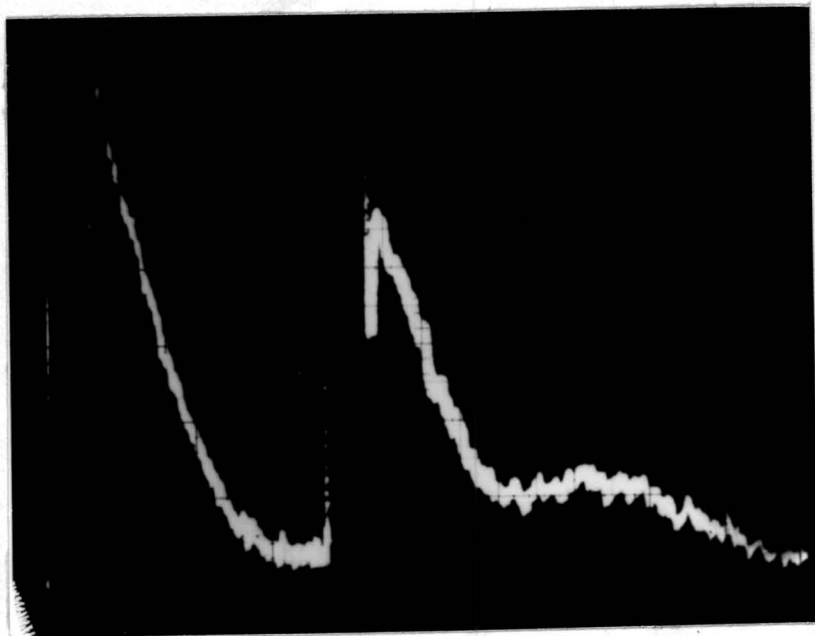

picture 5   Spin-echo and free induction decay in a homogenious exter-
nal field for a double pulse with condition $\theta = \omega_1 t_w < \pi/2$.
Total horizontal scale 100 μsec; total vertical scale 8 volt.

From the above result we can conclude that the behaviour of the free
induction decay is in accordance with the theory of Hahn.

D. The height of the echo as function of τ, the distance between the pulses.

According eq. 5.3.1. the maximum of the spin-echo is proportional to
exp $-2\tau/T_2$. On picture 6 the echo is photographed as function of τ. If we
plot the logarithm of the height of the spin-echo as a function of 2τ we obtain
a straight line. So the exponential decrease is obvious. The T_2, which is
obtained from the slope is about 42 µsec in this case. Only the double
pulse of the first echo is observed on the picture, because we covered
the double pulse when we photographed the other echo's on the screen of the
scope. The measurements were performed in an inhomogenious external field.
So we can conclude that the dependence of the height of the echo as function
of τ is in agreement with the theory of Hahn.
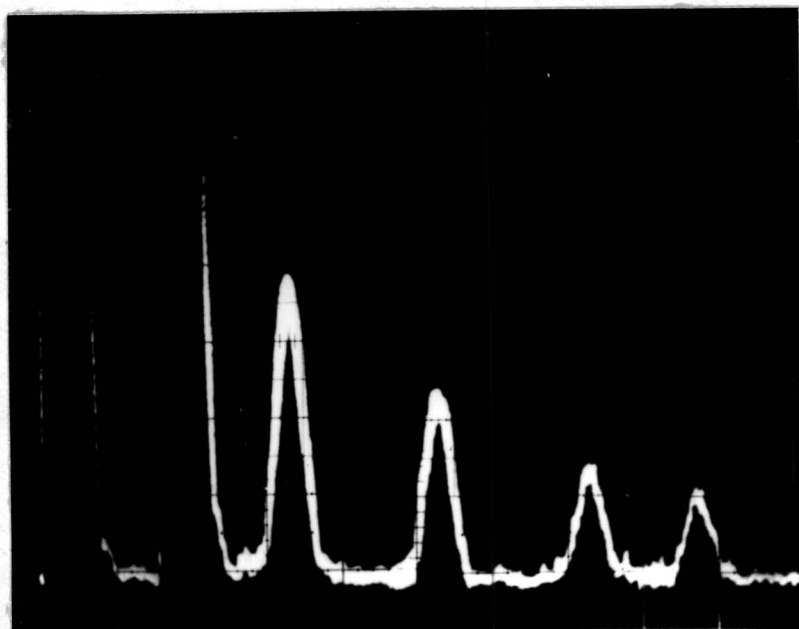
picture 6   Spin-echo as a function of the short delay. Total horizontal
scale 100 µsec; total vertical scale 8 volt.

5.4. Measurement of T_1

In this section we will describe the measurement of T_1 for paraffin.
It appeared that a comb of 20 pulses x 1.5 µsec with a distance between

the pulses of about 60 μsec could demagnetize the proton system of
paraffin. The pulse width of the double pulse was 1.5 μsec.
In table 1 the height of the spin-echo as function of the long delay
is given. If we plot the measured magnetization as a function of the long
delay (T), we obtain an exponential recovery as is shown in fig. 5.4.1.

long delay T (sec)	0.1	0.075	0.05	0.04	0.03	0.02	0.01	∞
V(T)~M_z(T) (volts)	3.7	3.4	2.6	2.15	1.85	1.3	0.5	4.5

table 1   Spin-echo amplitude as a function of the long delay T.
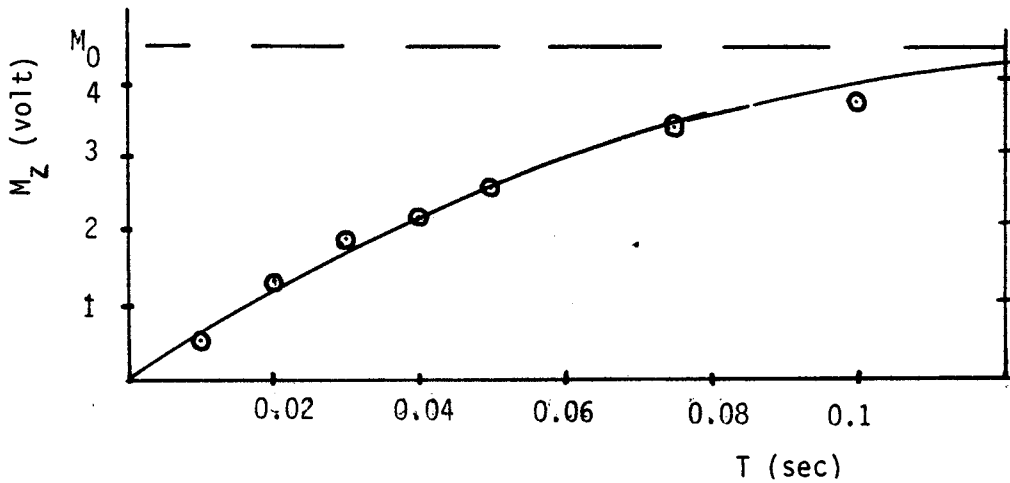
fig. 5.4.1.   Exponential recovery of the magnetization in paraffin.

For determining, however, the relaxation time T_1, it is much easier to graph
the experimental data in a different way. Therefore, we rewrite the equation
$M_z(t) = M_z(\infty)(1-e^{-t/T_1})$ as follows:

$$\ln\left(M_z(\infty) - M_z(t)\right) = -t/T_1 + \ln M_z(\infty) \qquad 5.4.1$$

So if we plot $\ln\left(M_z(\infty)-M_z(t)\right)$ against the long delay T we obtain a linear relation. The slope of the line is equal to the relaxation rate $(T_1)^{-1}$. (see fig. 5.4.2.).

long delay(sec)	0.1	0.075	0.05	0.04	0.03	0.02	0.01	0
$M_z(\infty)-M_z(T)$ (volts)	0.8	1.1	1.9	2.35	2.65	3.2	4.0	4.5

table 2 $M_z(\infty)-M_z(t)$ as a function of the long delay T.

We obtained a T_1 of 57 msec. Hahn reported a T_1 of 0.01 sec. So our result is of the same order of magnitude as that of Hahn.
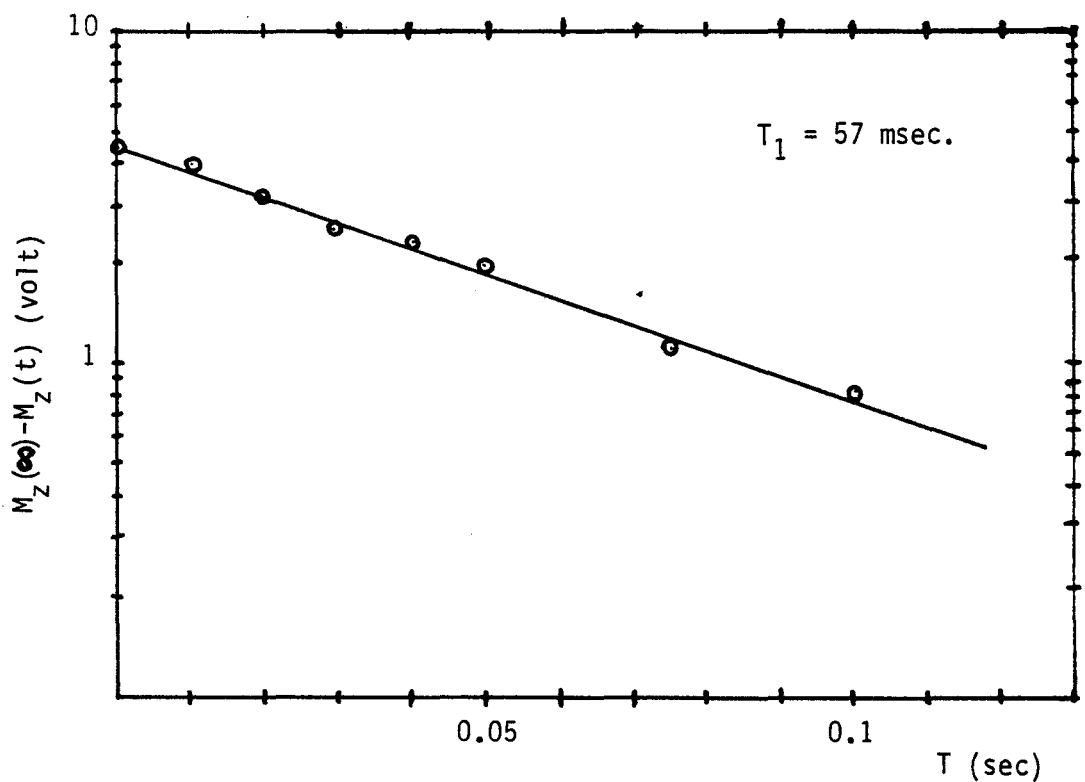
fig. 5.4.2   Logarithmic plot of $M_z(\infty)-M_z(t)$ against the long delay, T.

We always determine the T_1 in the way as described above.
Sometimes we can improve the echo signal by making the field more inhomo-

genious as will be shown below. In a homogenious field we can apply the second pulse, if the free induction decay is zero (see picture 4). If we apply it before the free induction decay is zero, we obtain a free induction decay after the second pulse, which can obscure the maximum of the spin-echo. In an inhomogenious field the free induction decay becomes smaller, and therefore we can apply the second pulse at a shorter t=τ. Because the height of the spin-echo is proportional to exp $-2\tau/T_2$ (section 5.2 D), the height of the spin-echo becomes larger (see picture 6). If we compare the height of the spin-echo in the homogenious field (picture 4) with the height of the first echo of picture 6 we observe the effect. In this way we can improve the signal to noise ratio of the spin-echo.

The nuclear spin lattice relaxation time T_1 is not expected to depend on the inhomogeneity of the magnetic field. We have checked this for paraffin by measuring T_1 as a function of the distance of the sample to the centre of the magnet (inhomogeneity of the field). In fig. 5.4.3 the results are shown.
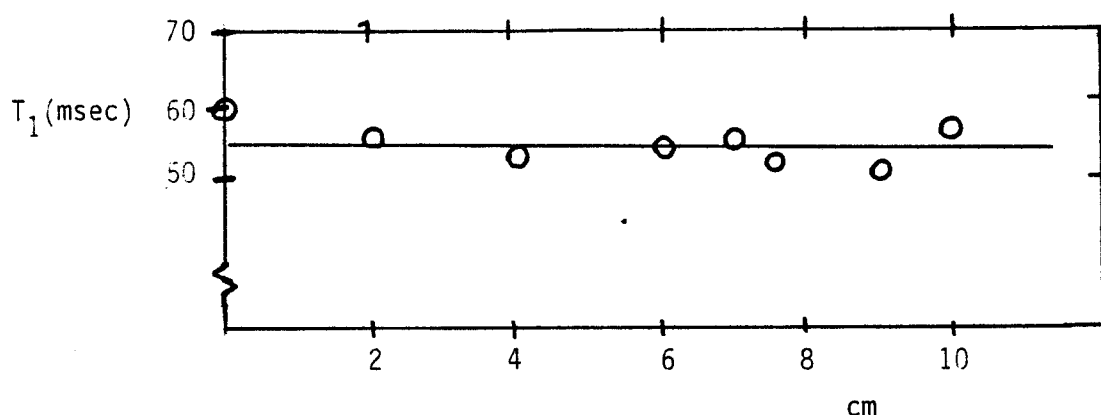

fig. 5.4.3. T_1 as a function of the distance of the sample to the centre of the magnet.

In fig. 5.4.4. the halfwidth of the spin-echo as a function of the distance of the sample to the centre of the magnet is plotted. Because the width of the echo is inversely proportional to the inhomogeneity of the magnetic field, we observe in fig. 5.4.4. that the inhomogeneity becomes larger as a function of the distance from the centre of the magnet.

From the above results we can conclude that the T_1 in paraffin does not depend on the inhomogeneity of the field.
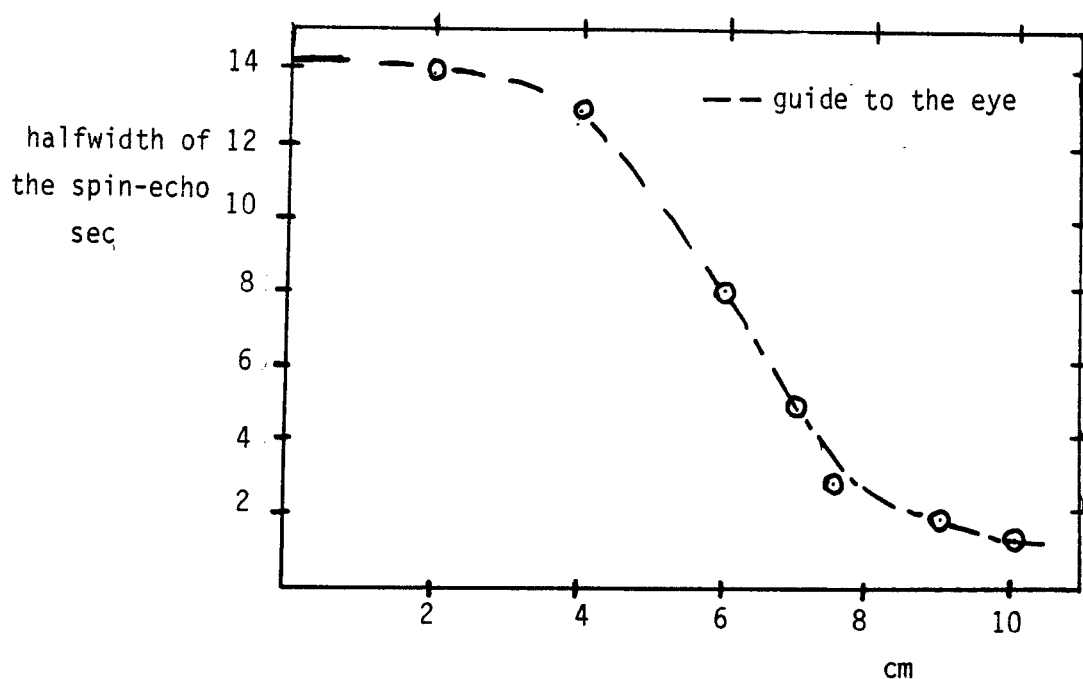
fig. 5.4.4.   The halfwidth of the spin-echo as a function of the dis-
tance to the centre of the magnet.

5.5. Discussion of some sources of inaccuracies in T_1

In section 5.4 we describe how we determine the spin-lattice relaxation
time. In this section we will discuss the experimental error in determining
T_1. We will divide this section in two parts. First we will discuss the
inaccuracy in determining the height of the spin-echo. Secondly the inaccuracy
in T_1 is treated.

The experimental error in the measurement of the height of the spin-echo
is determined by the signal to noise ratio of the spin-echo signal. By
repeating the experiment and averaging the height of the spin-echo we can
decrease the experimental error. In the case of paraffin the signal to
noise ratio was about 20.

We will now consider the experimental error in T_1. The T_1 is determined
from the slope of the logarithmic plot of $M(\infty)$ - $M(T)$ against the long
delay T as described in section 5.4. By estimating the uncertainty of the
slope of the line due to the spread of the points, we find an experimental
error in T_1 of about 5%. The spread in the points is larger than we would
expect from the signal to noise ratio of the individual spin-echo signals
(sum of the absolute error in $M(\infty)$ and $M(T)$ due to the signal to noise
ratio of the spin-echo).

Therefore we must conclude that there are other sources which cause an additional inaccuracy in $(M(\infty) - M(T))$. There are three sources that contribute to the additional inaccruacy in $(M(\infty) - M(T))$. First because of the non-linearity of the receiver the amplification factor of small signals is smaller. This gives an inaccuracy in the determination of $(M(\infty) - M(T))$ for short long delay times. Secondly it takes a relatively long time to measure T_1. If during the measurement the temperature, the external field or the pulse amplitude (amplitude of the alternating field) fluctuates, it affects the measured value of $(M(\infty) - M(T))$. Third the inaccuracy in the long delay T will contribute to the inaccuracy of $(M(\infty) - M(T))$. It is, however, difficult to give an estimation of the inaccuracy caused by these effects. In order to get an idea of the inaccuracy with which we can determine T_1 we measured several times the T_1 of paraffin under the "same" experimental conditions (external field, temperature).

The spread in the measured nuclear spin lattice relaxation times of paraffin was about 10%. This is reasonable for T_1 measurements (ref. 11).

5.6 Conclusions

From the results in section 5.2 we can conclude that the free induction decay and spin-echo in paraffin are in accordance with the analysis of Hahn (ref. 12).

From the measurement of T_1 in paraffin it follows that we can measure the T_1 with an accuracy of about 10%.

In conclusion we can say that the experimental set-up works satisfactory.

Chapter 6 Nuclear spin lattice relaxation time T_1 of ^{133}Cs and ^1H in RbFeCl$_3$.2H$_2$O and CsFeCl$_3$.2H$_2$O.

6.1 Introduction

During the last decade a considerable amount of theoretical and experimental research has been performed on the non-linear dynamics of one-dimensional magnetic systems. Many authors showed that the dynamics of a number of one-dimensional magnetic model systems is controlled by non-linear excitations (solitons) in a certain temperature and field region. Only recently Mikeska showed that the non-linear excitations can also be expected in a one-dimensional Ising-like antiferromagnet. (ref 13).

Because the experimental evidence of the existence of solitons is scarce, we thought it worthwhile to measure the relaxation time of ^1H and ^{133}Cs in the quasi 1d-Ising-like antiferromagnets RbFeCl$_3$.2H$_2$O (RFC) and CsFeCl$_3$.2H$_2$O (CFC) in order to verify the predicted influence of solitons.

After we treated the crystallographic and magnetic properties of RFC and CFC in section 6.2, we give in section 6.3 the results of T_1 measurements of ^1H and ^{133}Cs as a function of the temperature. In section 6.4 a preliminary interpretation on basis of the soliton theory is given.

6.2 Crystallographic and magnetic properties

The samples of RbFeCl$_3$.2H$_2$O and CsFeCl$_3$.2H$_2$O were grown at about 37° C of a solution of FeCl$_3$.4H$_2$O and RbCl or CsCl in a molar ratio of 3.2:1 and 3:1, respectively in a 0.03 N solution of HCl. In this way it was possible to grow large single crystals. The crystal axe are determined by X-ray diffraction (ref 18).

The crystallographic and magnetic structures have been determined from elastic neutron scattering experiments and nuclear magnetic resonance. The crystallographic space group is P$_{cca}$(orthorombic) (ref. 17). Along the a-axis the magnetic Fe^{2+}-ions are strongly coupled via a shared Cl$^-$-ion. This causes a strong magnetic interaction between two neighbouring moments along the a-axis. The magnetic coupling between the chains is weak because in the b-direction they are seperated by layers of Rb and Cs-ions and in the c-direction by hydrogen bonds (see fig 6.2.1).
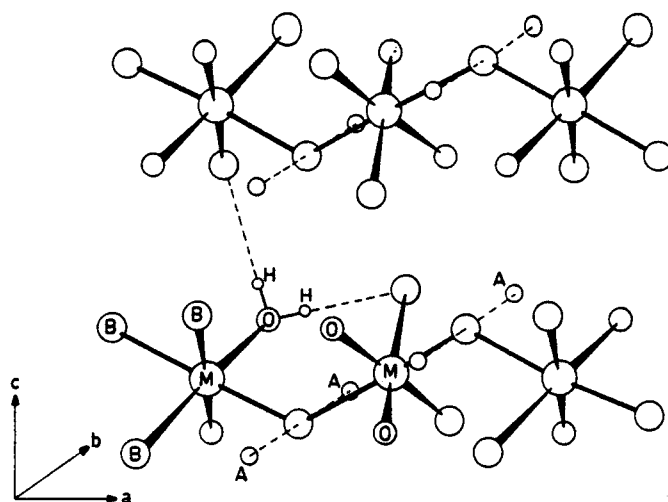
fig. 6.2.1   Schematic representation of the crystallographic structure
of $AMCl_3.2H_2O$ (A=Rb,Cs; M=Fe; B=Cl).

Because of the strong magnetic coupling between the moments along the
a-axis and the weak coupling along the b-axis and c-axis, we obtain
a quasi one-dimensional magnetic structure (magnetic chains along
the a-axis which are weakly coupled). Because of the weak interchain
interactions in RFC and CFC a three dimensional ordering occurs at T_N=
11.96 K and T_N=12.6 K, respectively. Magnetization measurements along
the c-axis exhibit in both compounds two successive metamagnetic tran-
sitions to a "pseudo" ferromagnetic state. In fig. 6.2.2. the phase
diagram of RFC for the external magnetic field H//c-axis is shown.(ref 19)
For CFC these transitions occur for the magnetic field H_{c1}=6.2 kOe and
H_{c2}=9.3 kOe, respectively at T=4.2 K.
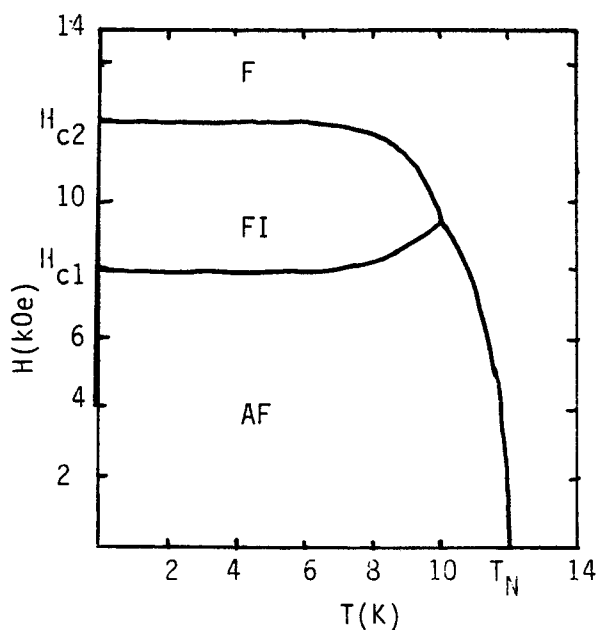
fig. 6.2.2   Schematic phase diagram
of $RbFeCl_3.2H_2O$ (H_{c1}=8.1
kOe; H_{c2}=12.4 kOe) .

In the ordered phase the magnetic moments are located in the ac-plane
at an angle of about 22° for RFC and 13° for CFC from the a-axis (ref 18).
The intrachain magnetic interaction is antiferromagnetic and Ising-like
for both compounds. Ising-like means that there exists a much stronger
interaction between one component of the magnetic moment (z-component)
than between the other two components.

In the paramagnetic phase ($T>T_N$) the properties of CFC and RFC are main-
ly determined by the properties of the individual chains. Therefore RFC
and CFC are known as pseudo one-dimensional Ising-like antiferromagnets.

6.3 T_1 of ^{133}Cs and ^{1}H as a function of the temperature

A   Preparation of the crystal.

In the first part of this section we will give a short description of
the preparation of the crystals of RFC and CFC. In the second part we
will present the results of the T_1 measurements.
The experiments to measure the nuclear spin lattice relaxation time
were performed on single crystals of the two isomorphic compounds RFC
and CFC. Around these crystals copperwire of 0.3 mm thick was wound
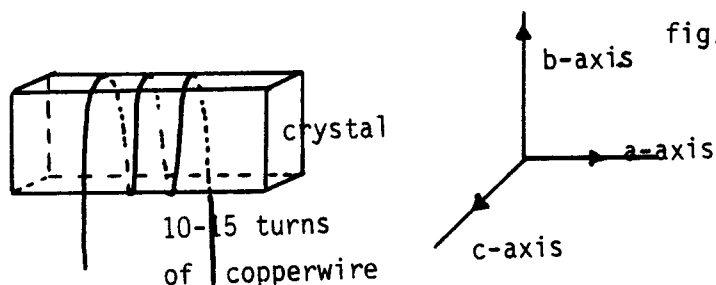in order to obtain a coil for the LC-circuit (shown in fig. 6.3.1.).

fig. 6.3.1 Coil in which the sample RFC or CFC is located. The crystals had a typical dimension of about 15x5x2 mm^3.

For the measurements of the T_1 of RFC and CFC we used a coil of about
10 -15 turns of copperwire and a fixed matching capacitor C_1 of 300 pF.
With this configuration we could tune the r.f. section with the variable
capacitor C_2 in the frequency range from about 30 to 50 MHz.

B   Results of the T_1 measurements

In this part of section 6.3 we will present the results of T_1 measurements
of ^{133}Cs and ^{1}H in RFC and CFC as a function of the temperature. These
measurements were performed in the paramagnetic phase ($T>T_N$).

In fig. 6.3.2 we plotted the measured ^{1}H nuclear spin lattice relaxation rate T_1^{-1} versus 1/T for CFC and RFC. From these figures it follows that there is a linear relationship between log $(T_1)^{-1}$ and 1/T in the temperature range 40 K<T<300 K.
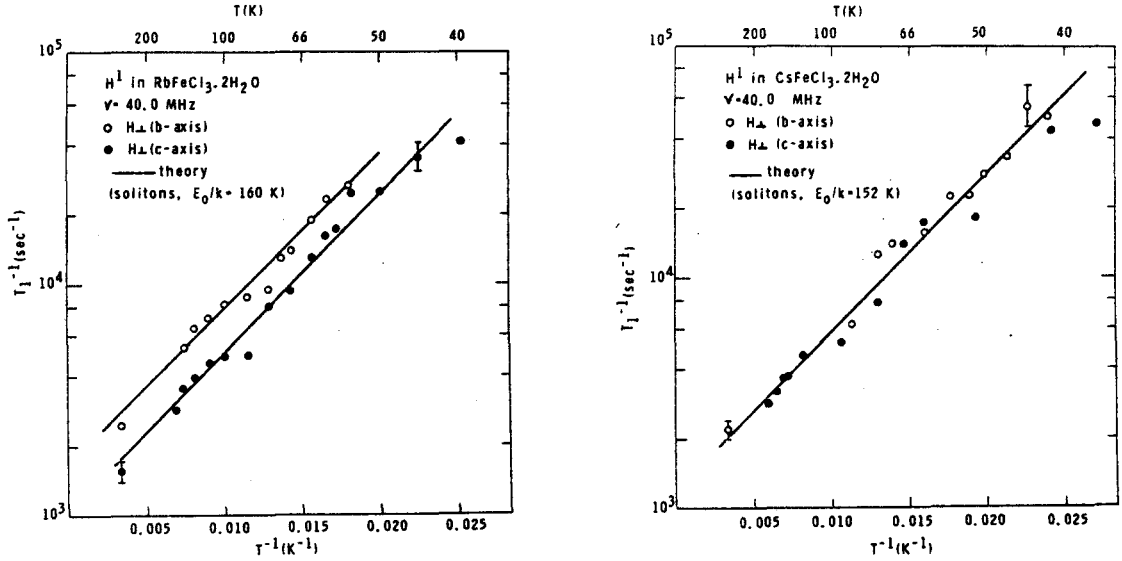

fig. 6.3.2 Nuclear spin lattice relaxation rate T_1^{-1} of ^{1}H of
RFC and CFC with the external field $\vec{H}//\vec{c}$ and $\vec{H}//\vec{b}$

At low temperatures (T<40 K) we could not measure the T_1 of protons in the paramagnetic phase because the spin-echo signal could not be observed.

In CFC we have also performed T_1 measurements on ^{133}Cs of which the results are shown in fig. 6.3.3 From this figure it follows that for temperatures T>20 K there is a linear relationship between $\log(T_1)^{-1}$ and 1/T.

In the next section a preliminary interpretation is given in which the linear relationship of log $(T_1)^{-1}$ with 1/T is explained by contributions to T_1 due to solitons.
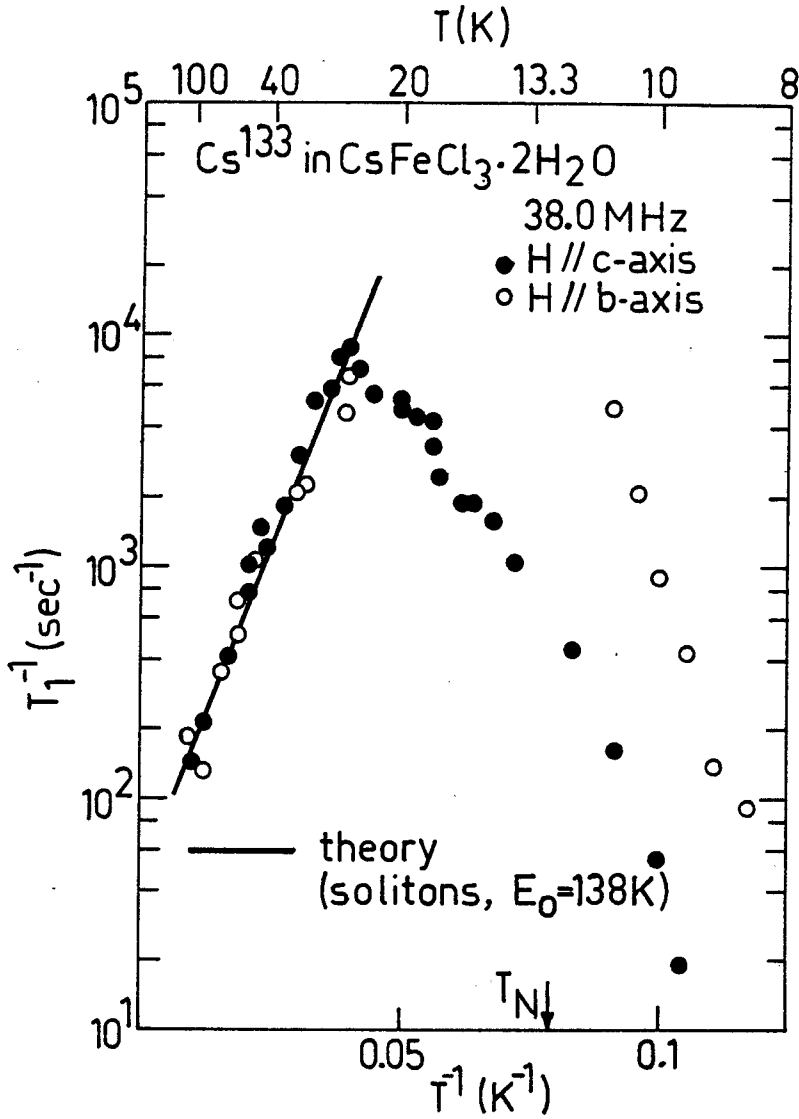
fig. 6.3.3 Nuclear spin lattice relaxation rate T_1^{-1} of ^{133}Cs of
CFC with the external field $\vec{H}//\vec{c}$ and $\vec{H}//\vec{b}$.

6.4 Preliminary interpretation on basis of the soliton theory.

In this section a preliminary interpretation of the measured data based
on the theory of Mikeska (ref 13) is given.
We describe the magnetic chain in CFC and RFC with the following
Hamiltonian:

$$\mathcal{H} = -J\sum_n \vec{S}_n \cdot \vec{S}_{n+1} + D\sum_n \left(S_n^z\right)^2 \qquad 6.4.1$$

The first term of the hamiltonian describes the exchange interaction
between two neighbouring spins. The second term is a single-ion term
which makes it energetically favourable for the spins to point along
the z-axis. For RFC the intrachain interaction is J/k_B=-5.4 K and the
single-ion anisotropy is D/k_B=-21 K. These values are determined from

the high temperature susceptibility data (ref 19) . For CFC no exact va-
lues for J/k_B and D/k_B are known. It is, however, assumed that J/k_B and
D/k_B have approximately the same values as for RFC (ref 20) .

Mikeska treated the spins as classical vectors. The two sublattices are
assumed anti-parallel. The angle θ of the direction of the sublattices
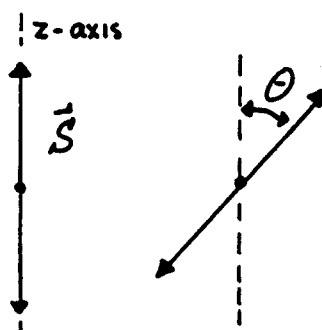with the preferential z-axis is defined as is shown in fig. 6.4.1.

fig. 6.4.1   Representation of the
two anti-parallel sublattices
with the polar angle θ .

Mikeska showed that when you apply the continuum limit to the Hamiltonian
(6.4.1), the following equation for the polar angle θ can be obtained:

$$\frac{\partial^2 (2\theta)}{\partial z^2} - \left(\frac{1}{c^2}\right)\frac{\partial^2 (2\theta)}{\partial t^2} = 2\left(\frac{D}{|J|}\right)\sin 2\theta \qquad 6.4.2$$

This is the Sine-Gordon equation for 2θ, with the mass-parameter $m = (2D/|J|)^{\frac{1}{2}}$
and the magnonvelocity c. This equation exhibits well known non-linear
soliton excitations. The form for these solitons is given by (ref 21):

$$\theta = 2 \arctan \left\{ \exp \pm m \gamma.(z - z_0 - vt)\right\} \qquad 6.4.3$$

where $\gamma = \left(\sqrt{1-v^2/c^2}\right)^{-1}$ and v, the velocity of the soliton, $\leq$ c.

We see that the soliton solution is physically a (moving) domain wall
which seperates the two degenerate ordered configurations of the anti-
ferromagnetic Ising chain, corresponding to $\theta = 0$ and π (see fig. 6.4.2.).
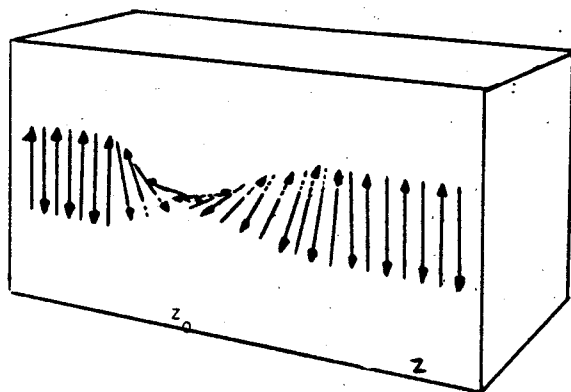

fig. 6.4.2   Moving domain wall

The rest energy of the soliton is given by:

$$E_0 = 2 S^2 (2D/|J|)^{1/2} \qquad 6.4.4$$

For RFC and CFC we have antiferromagnetic chains with S=2. With the intra-chain interaction J/k_B and the anisotropy term D/k_B we obtain for E_0/k_B=120 K.

It can be shown that the contribution of solitons to the nuclear spin lattice relaxation rate is given by (ref 22):

$$T_1^{-1} \sim exp[+E_0/k_B T] \qquad 6.4.5$$

From eq. 6.4.5. we see that there is a linear relation between $\log(T_1)^{-1}$ and $1/T$, of which the slope is given by E_0/k_B.

From the T_1 results of the protons for RFC and CFC we obtain E_0/k_B= 160±10 K and 152±10 K, respectively. From the T_1 of [133]Cs in CFC we obtain E_0/k_B= 138±10 K. If we compare these results with the theoretical prediction (E_0/k_B=120 K), we see that experiment and theory are in reasonable agreement. Therefore we conclude that at high temperatures (T>20 K) the T_1^{-1} can be explained by assuming a soliton theory. The T_1^{-1} results of [133]Cs in CFC at temperatures T<20 K can not be explained at the moment.

It should be emphasized that the interpretation of the experimental data as given above is still in a preliminary stage. We must also study the influence of other processes which may contribute to the nuclear spin lattice relaxation time, before we can be sure about the above interpretation. Furthermore we must check whether the Hamiltonian (eq. 6.4.1.) gives a good description of the magnetic chain in the described temperature range.

Appendix A TUNING PROCEDURE

In this appendix the tuning procedure of the r.f. receiver,
LC - circuit of the insert and r.f. generator will be des-
cribed. For tuning the r.f. receiver of the Matec and the
LC-circuit we make use of a r.f. signal generator (S.G.),
of which the output signal is amplitude modulated. As
mentioned already in chapter 4 the r.f. receiver gives the
envelope of the received r.f. signal at his output, which
is in the above case the amplitude modulation (a.m.). In fig.
A1 a schematic view of the connection of the equipment is
shown.
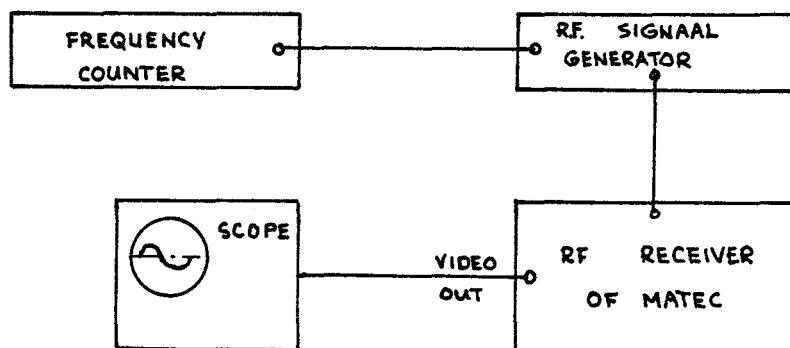
fig. A1 Connection of signal generator to r.f. receiver of
the Matec.

The frequency of the signal generator is measured with a
frequency counter. Next a 50% r.f. signal of the S.G. is
transmitted to the r.f. receiver of the Matec. The output
of this receiver is connected to a scope. We adjust the pre-
amplifier and the r.f. receiver tuning of the Matec until we
observe a maximum signal on the scope. It is recommended to
use the calibration data of the Matec which were determined
by the factory as a quide for this tuning. We can check the
tuning procedure by looking if a signal of some μV (4à5) of
the S.G. is still visible above the noise level.

If the receiver of the Matec is tuned at the right frequency
we can start   tuning the variable capacitor. of the LC-
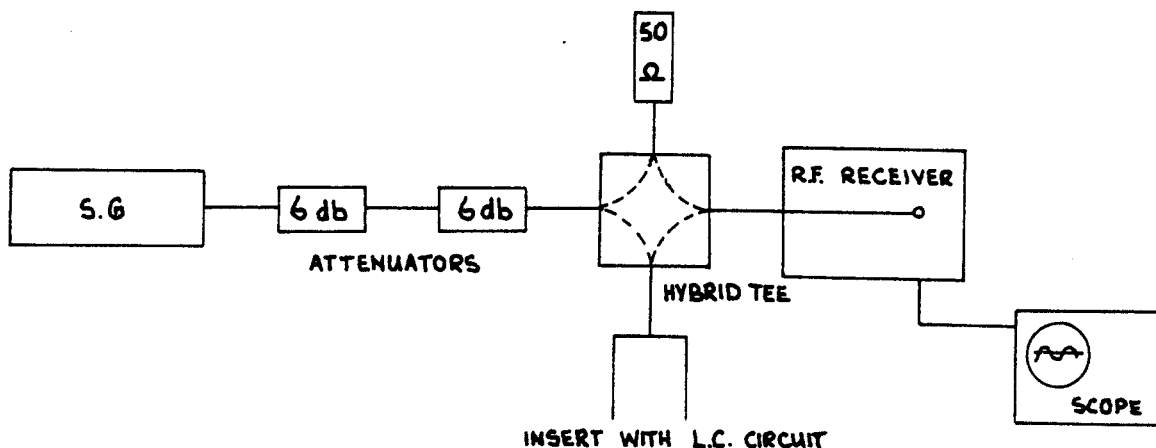circuit. For this we use a configuration as is shown in fig.
A2.

fig. A2 Schematic view of the configuration of the equipment
for tuning the LC-circuit.

The 50% a.m. signal of the S.G. is transmitted to the insert.
If the LC-circuit is completely mistuned most of the r.f.
signal is reflected and via the hybrid Tee and the r.f. re-
ceiver we obtain a maximum signal on the scope. By changing
the capacity of the LC-circuit we can find a minimum in the
reflected signal. In most cases the reflected signal in this
minimum is not equal to zero. This is only the case for the
frequency for which the impedance is matched rightly (see
chapter 4).
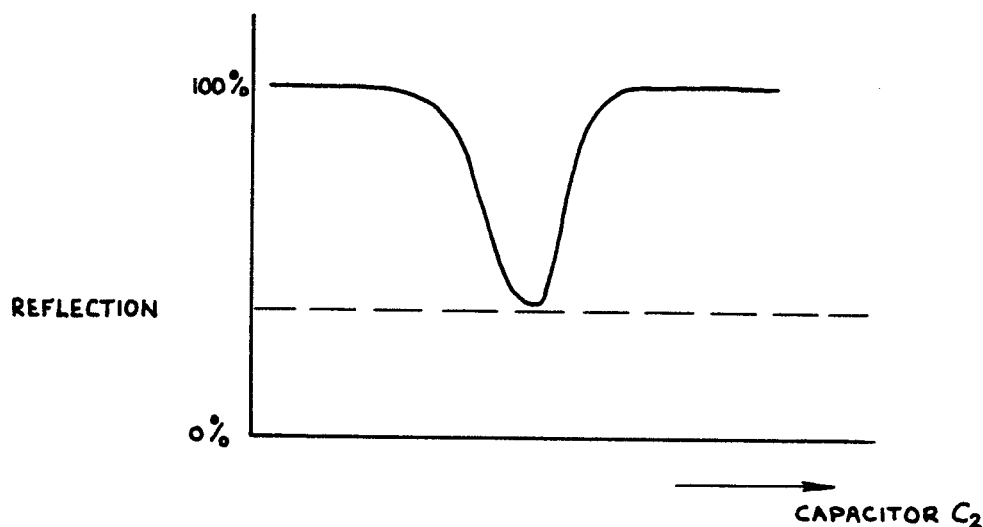
fig. A3 Reflection of r.f. signal (%) as function of the
variable capacity C_2

When the receiver and the insert are tuned we finally can
tune the r.f. generator of the Matec. For this we use the
normal experimental configuration (as is shown in fig. 4.1.1
of chapter 4). We now use however the internal modulation
program of the Matec, namely the single pulse mode with a
repetition rate of about 50 Hz. The r.f. monitor of the
Matec which gives attenuated r.f. pulses is connected to a
diode mixer. Also a signal generator is connected to this
diode mixer. The output of the diode mixer is connected to
the scope (fig A4).
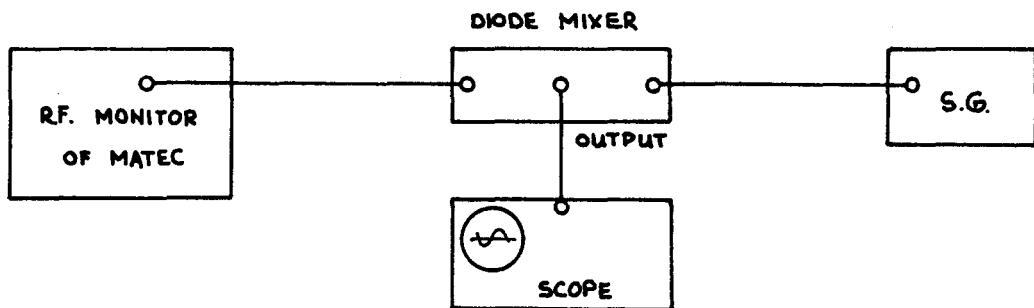
fig A4 Connection of the diode mixer to the Matec for tuning
       the r.f. generator.

If the r.f. generator is not tuned to the same frequency
as the S.G. we observe a pulse filled with a beat pattern
on the scope (as is shown in fig. A5(a)).If the generator
is tuned to the same frequency the beat pattern within the
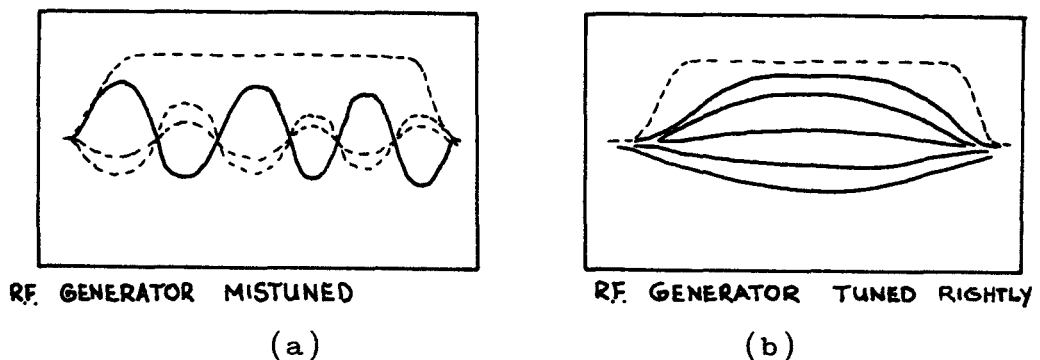pulse disappears (fig. A5(b)).

fig. A5 Output of the diode mixer. (a) mistuned r.f. generator
        (b) tuned r.f. generator.

After we finished the tuning procedure we can start the experiments. The modulation of the Matec must be switched to the external program to obtain the modulation program of the comb&double pulse generator.

If the external magnetic field and eventually the temperature are properly adjusted to obtain a nuclear resonance of the sample at the tuned frequency $(\omega_o = \gamma H_o)$, we can start with determining the condition for the double pulse and the comb for measuring the T_1.

First we apply only double pulses with a repetition rate larger than the relaxation time. If the pulse amplitude of r.f. generator is put to maximum and the receiver gain is made large, we may observe a spin-echo signal (see fig. A6)
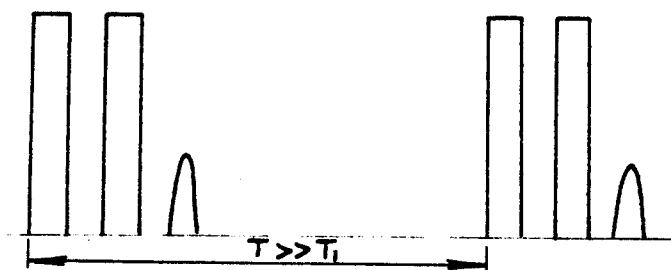

Fig. A6. Double pulse repeated at a slower rate than $1/T_1$. In this case the magnetisation is recovered to its equilibrium if the other double pulse is applied. For the right conditions of the double pulse we observe the maximum echo signal.

In this case it is very easy to adjust the pulse width t_w of the pulses, the pulse amplitude (mostly at maximum), the short delay T and the receiver gain to obtain an optimum spin echo signal.

In the same way we can repeate the comb & double pulse sequence as is shown in fig A7
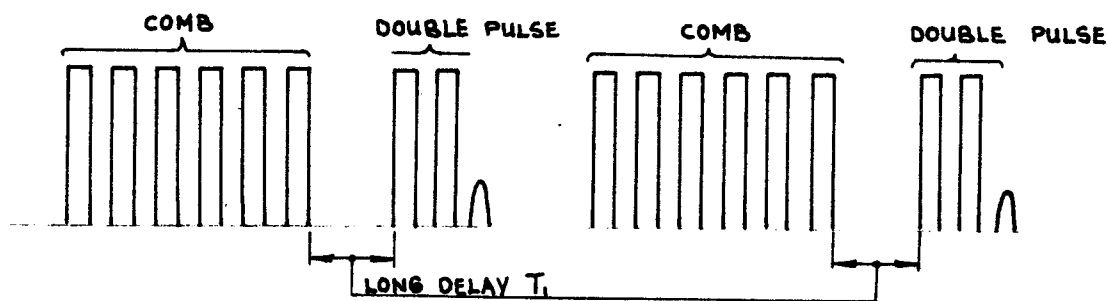
Fig. A7 Comb & double pulse sequence

In this case the duty cycle of the Matec must be observed
for high repetition rates (see § 4.2.). At low temperatures
the comb & double sequence can influence the temperature
stabilisation.

If we make the long delay T as short as possible (about 10
μsec which mostly is much shorter than T_1) we can adjust the
comb (the number of pulses, the pulse width of te pulses
and the distance between the pulses) to obtain a minimum
(if possible a zero) spin-echo signal. In this way we can
find the optimum conditions for the comb to demagnetize
(saturate) the nuclear spin system. If the comb and the
double pulse have the optimum condition we can start with
the T_1 measurements.

Appendix B Calculation of the magnetization component $M_{y'}(t)$.

In this appendix we calculate the magnetization component $M_{y'}(t)$ after the first pulse for the simple vector model (see section 3.3.2).

In the rotating coordinate frame the magnetic moment vector $M'(\Delta\omega)$ is defined as:

$$M'(\Delta\omega) = \left(M_{x'}(\Delta\omega),\ M_{y'}(\Delta\omega),\ M_z(\Delta\omega) \right)$$

We recall the Bloch equations and rewrite them for a rotating frame S', which rotates with ω_0, the centre frequency of the rectangular spectrum $g(\Delta\omega)$ (ref 12):

$$\frac{d M_{x'}(\Delta\omega)}{dt} + \Delta\omega\, M_{x'}(\Delta\omega) = \frac{M_{x'}(\Delta\omega)}{T_2}$$

$$\frac{d M_{y'}(\Delta\omega)}{dt} - \Delta\omega\, M_{y'}(\Delta\omega) + \omega_1 M_z(\Delta\omega) = -\frac{M_{y'}(\Delta\omega)}{T_2}$$

$$\frac{d M_z(\Delta\omega)}{dt} - \omega_1 M_{y'}(\Delta\omega) = \frac{-(M_z(\Delta\omega) - M_0)}{T_1}$$

$\omega_1 = \gamma H_1$ is only different from zero during a r.f. pulse

After the $\pi/2$-pulse, the $M_{y'}(t,\Delta\omega)$ is obtained from the above Bloch equations. Because t_w (duration of the pulse) is much shorter than $1/(\Delta\omega)_{1/2}, T_2, T_1$, we can neglect it and the initial condition for $M_{y'}(0,\Delta\omega)$ is given by $M_{y'}(0,\Delta\omega) = -M_z\, g(\Delta\omega)$
The solution for $M_{y'}(t)$ is:

$$M_{y'}(t,\Delta\omega) = -M_z\, g(\Delta\omega)\, \cos\Delta\omega t\ \exp^{-t/T_2}$$

The resulting $M_{y'}(t)$ is found by integration over all frequencies $\Delta\omega$:

$$M_{y'}(t) = -\frac{M_z}{2(\Delta\omega)_{1/2}}\, \exp^{-t/T_2} \int_{-(\Delta\omega)_{1/2}}^{+(\Delta\omega)_{1/2}} \cos(\Delta\omega t)\, d(\Delta\omega)$$

$$= -M_z\, \exp^{-t/T_2}\ \frac{\sin(\Delta\omega)_{1/2}\, t}{(\Delta\omega)_{1/2}\, t}$$

Appendix C   Fourier spectrum of the r.f. pulse

Because the r.f. pulses of the double pulse (and of the comb) have a very small pulse width (μ sec) the frequency spectrum can become large (of the order of 100 kHz), although the pulses are filled with a r.f. carrier of one frequency. If we approximate the r.f. pulse by an ideal rectangular pulse the Fourier transform is given by the sinc-function (see fig. C1),(ref 23):
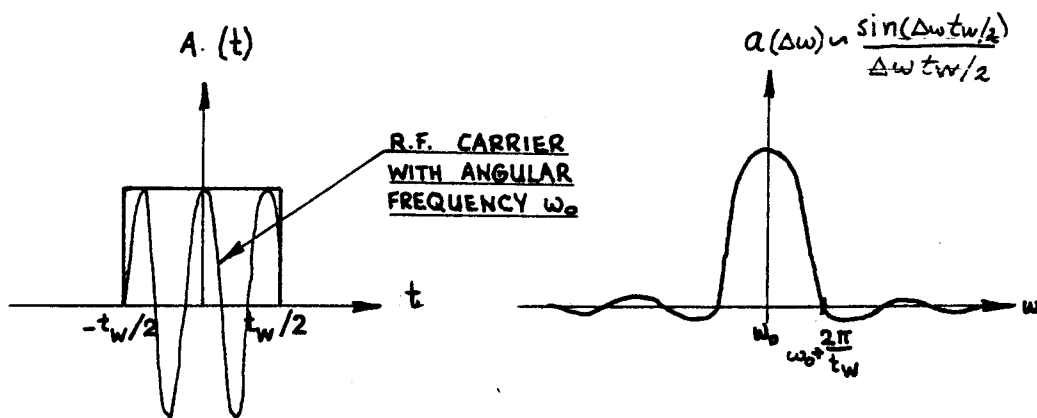

fig. C1   A pulse modulated r.f. signal and the corresponding frequency spectrum.

References

ref 1 Slichter, "Principles of Magnetic Resonance", Harper&Row, New York (1963), p.4-8.

ref 2 idem ref 1, p. 10-12.

ref 3 T. Tinus, private communication.

ref 4 G.J. Gerritsma, Ph. D. Thesis, Twente.

ref 5 D. Beeman, P. Pincus, Phys. Rev. B, 166, 359 (1968).

ref 6 H. Nishihara, W.J.M. de Jonge and T. de Neef, Phys. Rev. B 12, 5325 (1975).

ref 7 A. Abragam, "The principles of nuclear magnetism", Claredon Press, Oxford (1961), p. 14.

ref 8 idem ref 7, p. 44.

ref 9 idem ref 7, p. 20-22.

ref 10 idem ref 1, p. 12-13.

ref 11 H. Nishihara, private communication.

ref 12 E.L. Hahn, Phys. Rev. 80, 580 (1950).

ref 13 H.J. Mikeska, J. Phys. C: Solid State Phys. 13, 2913 (1980).

ref 14 Operating and Instruction manual of the Matec (model 6600).

ref 15 K. Kopinga and J. Millenaar, Internal Report T.H. Eindhoven (1978).

ref 16 A. Breuls, Internal Report T.H. Eindhoven (1980).

ref 17 J.A.J. Basten, Q.A.G. van Vlimmeren and W.J.M. de Jonge, Phys. Rev. B. 18, 2179 (1978).

ref 18 J. Buys, Internal Report T.H. Eindhoven(1977).

ref 19 Q.A.G. van Vlimmeren, Ph. D. Thesis, T.H. Eindhoven (1979).

ref 20 T. Tinus, private communication.

ref 21 A. Barone, F. Esposido, C.J. Magnee, A.C. Scott, Riv. Nuovo
ref 21 Cimento 1, 227 (1971).

ref 22 R.C. Thiel, H. de Graaf, L.J. de Jongh, Phys. Rev. Letters 47, 1415 (1981).

ref 23 E. Fukushisma, S.B.W. Roeder, "Experimental pulse NMR", Addison-Wesley Publishing Company (1981), p. 51.